

# Exploiting correlations in multi-coincidence Coulomb explosion patterns for differentiating molecular structures using machine learning

Anbu Selvam Venkatachalam,<sup>1</sup> Loren Greenman,<sup>1</sup> Joshua Stallbaumer,<sup>1</sup>  
Artem Rudenko,<sup>1</sup> Daniel Rolles,<sup>1</sup> and Huynh Van Sa Lam<sup>1,\*</sup>

<sup>1</sup>*James R. Macdonald Laboratory, Department of Physics,  
Kansas State University, Manhattan, KS 66506, USA*

(Dated: September 5, 2025)

Coulomb explosion imaging (CEI) is a powerful technique for capturing the real-time motion of individual atoms during ultrafast photochemical reactions. CEI generates high-dimensional data with naturally embedded correlations that allow mapping the coordinated motion of nuclei in molecules. This enables reliable separation of competing reaction pathways and makes this approach uniquely suited for characterizing weak reaction channels. However, rich information contained in experimental CEI patterns remains largely underexploited due to challenges in visualizing correlations between multiple observables in multi-dimensional parameter space. Here we present a new approach to CEI of intermediate-sized polyatomic molecules, detecting up to eight ionic fragments in coincidence and leveraging machine-learning-based analysis to identify patterns and correlations in the resulting high-dimensional momentum-space data, enabling robust molecular structure identification and differentiation. Our approach provides high-dimensional background-free data encoding exceptionally rich structural information and establishes an automated, scalable framework for extracting insightful information from the data. As a demonstration, we apply this method to image and distinguish dichloroethylene isomers, showcasing its potential for broader applications in molecular imaging. Our results pave the way for channel-specific analysis of ultrafast structural dynamics in chemically relevant systems, particularly for disentangling mixed reaction pathways and detecting contributions from weak channels and minority species.

The ability to visualize and characterize molecular structures has long been a cornerstone of scientific discovery, enabling researchers to elucidate mechanisms of chemical reactions, design novel materials, and develop targeted therapeutics. Recent advances in ultrafast imaging techniques have revolutionized our capacity to directly observe the transformation of molecular structures during chemical reactions, shedding light on fundamental processes such as bond breaking, isomerization, and electronic excitation. These developments provide foundational knowledge spanning multiple scientific disciplines [1–8].

Coulomb explosion imaging (CEI) [9] has emerged as a powerful and promising technique for tracking time-dependent molecular motions when coupled with ultrafast light sources in a pump-probe scheme [10]. It provides excellent temporal resolution, high sensitivity to light atoms, and direct access to three-dimensional (3D) information, even though the inversion to real-space molecular geometries is not always possible. In time-resolved CEI, the molecule of interest can be ionized using an intense laser [10–15] or X-ray [16–19] pulse, stripping away multiple electrons and leaving the molecule in highly charged states. The resulting Coulomb repulsion between positively charged fragments causes the molecule to explode, and the measured momenta of these fragments encode information about the molecular structure. CEI is particularly powerful when the probe radiation can break all the bonds and fully dissociate the molecule

into atomic ions, and all resulting ions are detected in coincidence. In such cases, for every single shot, CEI yields information potentially sufficient to determine the absolute structures of polyatomic molecules, including enantiomers [12, 20], and provides molecular frame information. However, detecting all ionic fragments resulting from the complete breakup of the molecule in coincidence is experimentally challenging. As a result, while CEI has been highly successful in imaging small molecules [10, 21–31], its application to larger molecules has yielded only limited/partial structural information. Recent advances have addressed this limitation, demonstrating that CEI can image detailed 3D structures of gas-phase molecules with approximately ten atoms by leveraging coincidences from a subset of ions [14, 17–19, 32]. However, this method faces challenges when signals of interest are weak or contaminated by background noise.

Another current limitation of CEI applications for polyatomic molecules stems from the inherent complexity and multidimensionality of the data. Coincident CEI—whether performed in complete or incomplete mode—relies on analyzing the 3D momentum vectors of all detected ions. Whenever three or more ions are detected in coincidence, the number of correlated observables that could be important for characterizing structures or dynamics of interest becomes very large, particularly when both laboratory-frame and molecular-frame quantities are considered [15]. Although several efficient and standardized data representation schemes have been developed for three-particle analysis—such as Newton diagrams for visualizing momentum correlations, Dalitz plots for energy partitioning among fragments [33], and

\* huynhlan@ksu.edu

more recently, the “native-frame” approach using conjugate momenta in Jacobi coordinates [34, 35]—these methods only partially capture the rich information embedded in CEI datasets even for the three-body breakups. As the number of detected fragments increases, especially when pump-probe time delays are included [18, 36], the parameter space grows rapidly. Observables defined and visualized by conventional human-driven analysis typically sample only a narrow portion of this space, leaving much of the correlated structural and dynamical information unexplored.

In this work, we address these limitations by pushing CEI with kinematically complete coincidence imaging into the regime of intermediate-sized molecules. Specifically, we demonstrate that the detection of up to eight-ion coincidences is feasible with currently available tabletop laser and detector technology, extending previous reports on five-atom molecules [9, 12, 37–40]. In such “complete” CEI measurements, where all created ionic fragments are detected in coincidence, strict momentum conservation ensures background-free data, allowing for the unambiguous identification of weak reaction pathways [41] and contributions from minority species such as dimers in dilute samples. Imaging all atoms in a polyatomic molecule in a single shot provides extraordinarily rich structural information, opening new opportunities for investigating time-resolved structural dynamics of photoinduced reactions of chemically relevant organic molecules with unprecedented details.

As a second major step forward, we present a new analysis framework based on machine learning (ML) to help interpret the high-dimensional data from multi-coincidence CEI. Each multi-coincidence event generates a multi-vector data point (three momentum components for each fragment ion), and the distribution of such events forms a complex dataset that encodes detailed information about the structure and subtle correlations between atomic ions. As mentioned earlier, extracting meaningful insights from such data typically requires laborious analysis of the momentum distributions and manual gating on specific projections guided by human intuition, which can be challenging and prone to bias. We demonstrate that ML algorithms can efficiently recognize and exploit momentum-space patterns and correlations corresponding to distinct molecular geometries. Furthermore, we introduce a quantitative approach to determine which features in the high-dimensional CEI data are the most critical for differentiating similar structures. As molecular size increases, momentum correlations grow combinatorially more complex, making ML particularly well suited for handling such datasets. By leveraging the readily available ML toolbox, we establish an automated and scalable analysis framework for structural imaging using multi-coincidence CEI.

As a demonstration, we apply these advancements to imaging and differentiating isomer structures, which is a critical subject of investigation across multiple fields, including chemistry, pharmacology, biochemistry, and ma-

terial science [42–45]. Although isomers share the same molecular formula, their structural differences lead to distinct physical and chemical properties that affect their behavior. For example, in pharmacology, small structural changes can result in dramatically different biological effects, as exemplified by the enantiomers of thalidomide, where one form is therapeutic and the other harmful [42]. CEI has previously been used to image chiral [12, 20, 46–49], geometric isomer [32, 50–53], and conformer [54] configurations of molecules. In this work, we investigate the isomers of dichloroethylene (DCE). First, we present CEI of 1,2-DCE, where the molecule fully dissociates into six atomic ions, and the full 3D momenta of all fragments are detected in coincidence. Second, using unsupervised learning, we demonstrate that coincident CEI data can be automatically separated into distinct clusters corresponding to different isomers on an event-by-event basis. Third, we employ supervised learning to determine which projections in high-dimensional CEI data are most important for distinguishing isomeric structures and similar configurations that can arise during photochemical reactions. Finally, we extend CEI to achieve up to eight-ion coincidences in isoxazole. Looking forward, the methods developed here pave the way for time-resolved investigations of larger molecular systems with all-atoms imaging and automated data interpretation.

## RESULTS AND DISCUSSION

Figure 1(a) presents the ion momentum image (Newton plot) of the *cis*-DCE molecule, constructed from six-fold coincidence events in which all singly charged fragment ions (two  $\text{H}^+$ , two  $\text{C}^+$ , and two  $^{35}\text{Cl}^+$ ) are detected. The reference frame is defined by the momenta of the two  $\text{Cl}^+$  ions (see the caption for details), with the  $\text{C}^+$  and  $\text{H}^+$  ions plotted in this frame. A similar Newton plot for the *trans*-DCE isomer is shown in Figure 2(a). In this configuration, the momentum vectors of the two  $\text{Cl}^+$  ions are nearly back-to-back, making their vector sum and consequently the  $p_x p_y$  plane less well-defined (see SI, Fig. S1). To mitigate this, we define the  $p_x p_y$  plane for *trans*-DCE using the vector difference between the momenta of the two  $\text{C}^+$  ions. The resulting momentum image reveals distinct, well-separated features corresponding to each atomic fragment. This is a clear example demonstrating that one frame of reference is not necessarily suitable for all different molecular structures. One needs to combine different representations to elucidate different reaction dynamics.

The maxima in the momentum distributions of the chlorine, carbon, and hydrogen ions are well-localized, encoding the structure information of the underlying molecular geometry. Figures 1(b) and 2(b) present the results of classical Coulomb explosion simulations, assuming point charges, purely Coulombic potential, and instantaneous ionization [14, 55]. The simulations be-

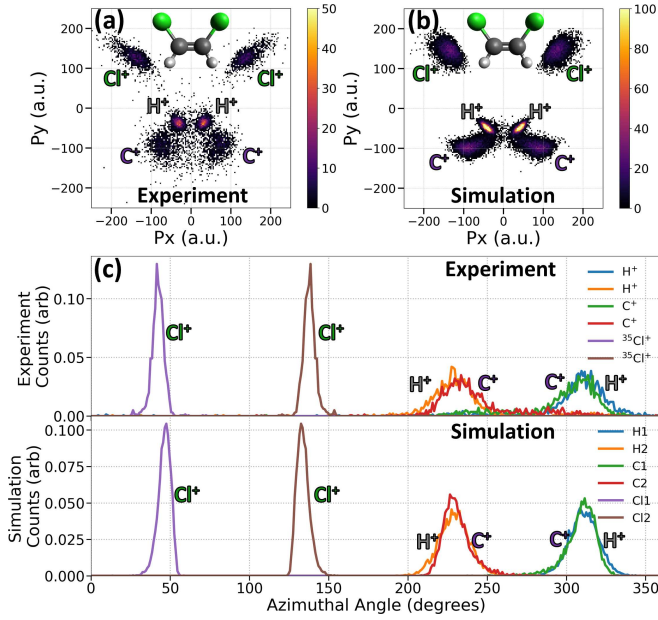


FIG. 1. (a) Measured and (b) simulated CEI patterns (Newton plots) of *cis*-DCE from the ( $H^+$ ,  $H^+$ ,  $C^+$ ,  $C^+$ ,  $^{35}Cl^+$ ,  $^{35}Cl^+$ ) 6-fold coincidence channel. The insets show ball-and-stick model views in the molecular plane. For each event plotted here, the coordinate frame is rotated such that the vector difference between the two  $Cl^+$  momenta unit vectors points along the  $p_x$  axis and the bisector between them lies in the upper  $p_x p_y$  plane. The momenta of  $C^+$  and  $H^+$  are plotted in this coordinate frame. Panel (c) shows the experimental (top) and simulated (bottom) distributions of azimuthal angle for each ion (integrated over momentum magnitude). The azimuthal angle is measured counter-clockwise from the  $p_x$  axis.

gin with the neutral molecule in its equilibrium geometry, with Gaussian-distributed spatial displacements and total kinetic energy (randomly partitioned among the atoms) introduced to account for the initial distribution and broadening effects due to atomic motion during the ionization process. Here, the spatial deviation of 0.25 Å and a total kinetic energy of 500 meV are used to match the width of the experimental distributions. This model successfully reproduces key features of the experimental momentum distributions, capturing the separation and localization of the fragment ions with good accuracy. This agreement suggests that the measured momentum distributions faithfully reflect the molecular structure near the equilibrium of the neutral molecule.

To provide a more quantitative comparison between experiment and simulation, Figures 1(c) and 2(c) show the azimuthal angle distributions for each ion, obtained by integrating over the radial momentum coordinate. The experimental (top) and simulated (bottom) distributions exhibit excellent overall agreement, indicating that the Coulomb explosion model effectively captures the correlated angular relationships between fragment ions.

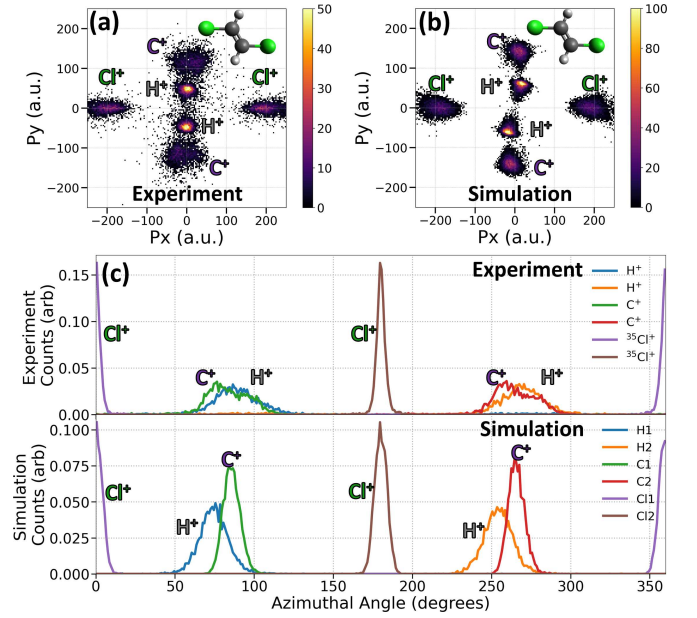


FIG. 2. The same as Fig. 1 but for *trans*-DCE molecule. In this case, the coordinate frame for each event is aligned such that the difference vector between the two  $Cl^+$  momenta is parallel to the  $p_x$  axis. The  $p_x p_y$  plane is established using the vector difference of the two  $C^+$  momenta.

These results validate the ability of the simulation to model the Coulomb explosion dynamics of the DCE molecules with high fidelity. The complete coincidence detection of the full 3D momenta of all atomic ions essentially provides background-free data, where the observed experimental features for the 6-body coincidences are as well-defined as those in the simulation. This level of agreement is not always achieved in cases of incomplete coincidence detection, where experimental distributions are broadened by contamination from false coincidence or different final charge states (see SI, Fig. S2).

We also perform CEI on a sample containing a mixture of *cis* and *trans* isomers. Fig. 3(a) shows the momentum pattern of this data after rotating each event to a common frame of references defined by the two  $Cl^+$  momenta as in Fig. 1(a,b). Compared to the data of only the *cis* isomer in Fig. 1(a), new features belonging to the *trans* isomer appear. Some features are well separated from the *cis*-DCE pattern, while some overlap. In order to automatically separate events corresponding to *cis* and *trans* isomers from the mixture, we first perform data reduction to reduce this data of eighteen dimensions into two dimensions, as shown in Fig. 3(b). Here, we choose to use UMAP (Uniform Manifold Approximation and Projection) [56]—which constructs a high-dimensional graph representation of the data based on topology and then optimizes a low-dimensional graph to be as structurally similar as possible—for data reduction due to its ability to handle nonlinear patterns and its computational efficiency. A comparison between UMAP and other popular data reduction techniques is provided in Methods and

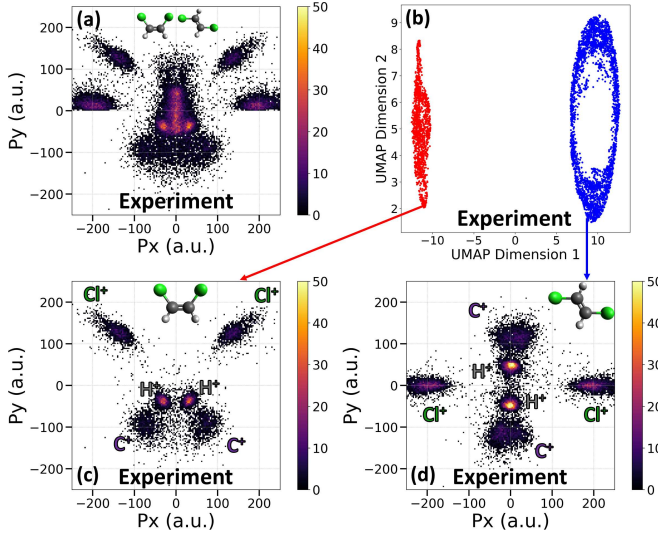


FIG. 3. Automatic separation of *cis* and *trans* isomers events from experimental data of a mixture. (a) Newton plot of a mixture of isomers. (b) Data reduction using UMAP, where the events are colored according to their labels obtained from clustering using the HDBSCAN method. (c) and (d) are Newton plots of *cis* and *trans* molecules after separation, respectively. The Newton plots of the mixture (a) and of the *cis* isomer (c) use the same reference vectors as defined in Fig. 1. For the *trans* isomer in (d), the reference frame is described in Fig. 2.

the SM. After the dimensionality reduction, the data is clearly separated into two groups. Events from these two groups are correctly clustered using HDBSCAN (Hierarchical Density-Based Spatial Clustering of Applications with Noise) [57]—an algorithm that builds a hierarchy of clusters by varying the density threshold and extracts the most stable clusters while automatically labeling low-density regions as noise—and then colored according to their cluster labels.

We then plot the momentum images of these events separately in Fig. 3(c) and Fig. 3(d) for events from clusters labeled red and blue, respectively. The momentum image in Fig. 3(c) closely resembles that in Fig. 1(a), indicating that these events correspond to the *cis* isomer. Meanwhile, the momentum image in Fig. 3(d) exhibits a distinct pattern that aligns well with events from the *trans* molecules, as seen in Fig. 2(a). The excellent agreement between momentum images of events from these two clusters and data collected with individual isomers confirms that the data reduction and clustering algorithms above have been able to accurately separate *cis* and *trans* isomers on an event-by-event basis, automatically.

Now that the two isomers have been accurately clustered and labeled, we turn to a supervised ML approach to quantitatively assess which features contribute most to the differences between *cis* and *trans*. The key motivation for this analysis arises from the limitations of experimental observables, especially when used individu-

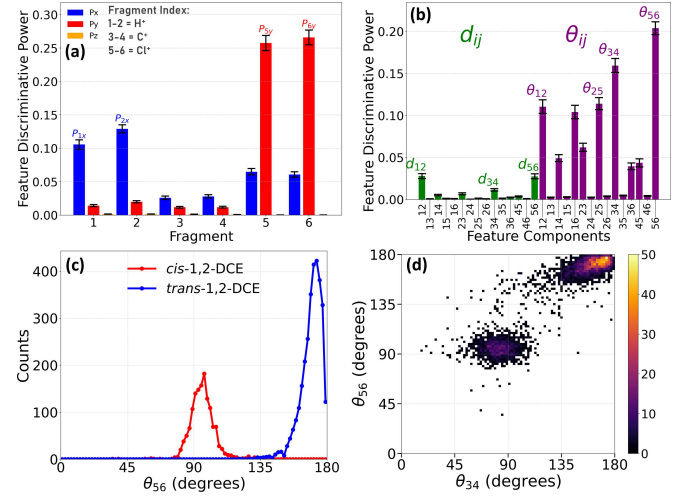


FIG. 4. Discriminative power analysis for distinguishing *cis*- and *trans*-DCE isomers. Fragment indices are assigned as follows: 1–2 =  $H^+$ , 3–4 =  $C^+$ , and 5–6 =  $Cl^+$ . Panel (a) highlights key features that contribute to the distinction between the two isomers for individual momentum components ( $p_1$  to  $p_6$  in X, Y, and Z directions) obtained from the Random Forest classifier, where larger values indicate greater discriminative power. Panel (b) is similar to (a) but for different features  $d_{ij} = |\vec{p}_j - \vec{p}_i|$  (green) and  $\theta_{ij} = \angle(\vec{p}_i, \vec{p}_j)$  (purple) (see text for more description). Panel (c) presents the experimental distribution of the angle between the two  $Cl^+$  ions for both *cis* (red) and *trans* (blue) isomers. Panel (d) is the two-dimensional angle correlation plot between  $\theta_{34}$  and  $\theta_{56}$ .

ally, in capturing the structural differences between isomers. While our current data shows a clean separation between the two isomers, it is not always guaranteed. If many closely similar configurations coexist, isomers might appear as different parts of one big cluster, making differentiating them difficult, especially when the *reduced dimension* is not always readily interpretable. Our following analysis provides insights into how to construct meaningful observables to effectively differentiate similar structures. In particular, we employ the Random Forest Classifier [58]—an ensemble learning method that builds multiple decision trees using bootstrap samples and random feature subsets, then aggregates their votes to produce a more accurate and robust classification—to evaluate the discriminative power of different features. Features with high discriminative power can easily tell the two isomers apart, while ones with low discriminative power cannot cleanly separate the two. We perform this analysis for components of the momentum vectors in Cartesian coordinates and also internal momentum coordinates such as the angle between two momentum vectors and the magnitude of the vector differences.

Figure 4(a) presents the discriminative power analysis obtained from a Random Forest classifier trained to distinguish between the *cis* and *trans* isomers based on their measured Coulomb explosion momenta in the Cartesian representation [shown in Fig. 3(a)]. This result shows



that the X and Y components of the fragment momenta are more informative than the Z component, which is expected from the planar symmetry of 1,2-DCE isomers. The effectiveness of  $p_{5y}$  and  $p_{6y}$  (vertical momenta of the chlorines) and  $p_{1x}$  and  $p_{2x}$  (horizontal momenta of the protons) in separating the isomers can be seen in Fig. 3(a) (and also Fig. S16 of the SI).

While the analysis in Cartesian coordinates provides insight into how momentum-space observables correlate with molecular structure, a more intuitive description that involves the momentum internal coordinates, such as  $d_{ij}$  and  $\theta_{ij}$ , can be used. Here,  $d_{ij} = |\vec{p}_j - \vec{p}_i|$  is the modulus of the difference between two momentum vectors and  $\theta_{ij} = \angle(\vec{p}_i, \vec{p}_j)$  denotes the angle between them. These features are invariant to translation and rotation, offering a robust description of the structural information independent of spatial orientation. These features have been successfully used to track changes in bond lengths [23, 59, 60] and bond angles [15, 46] in the nuclear wave packet dynamics of molecules.

The result, shown in Fig. 4(b), reveals that the angles ( $\theta_{ij}$ ) exhibit much stronger discriminative power compared to the magnitudes ( $d_{ij}$ ). This is because isomers have similar bond lengths, which are the main factor in determining the momentum magnitude (through the Coulomb interactions).  $d_{ij}$  is more important when significant bond-length differences arise, such as during dissociation. Here, the angle correlations between fragment momenta — notably those involving pairs of  $H^+$ ,  $C^+$ , and  $Cl^+$  ions — serve as strong distinguishing factors between the isomers. While the role of  $Cl^+$  and  $H^+$  ions was evident in Cartesian coordinates, this representation highlights the significant contribution of the angle between  $C^+$  fragments, providing additional structural cues for isomer differentiation.

Figure 4(c) shows the distribution of the angle between two  $Cl^+$  fragments ( $\theta_{56}$ ). This quantity was previously identified as the defining structural characteristic of *cis* and *trans* configurations in similar cases [50, 52, 53], which we confirm and quantify as the strongest single discriminator for the two isomers in our analysis. In our current data, this feature by itself can separate the two isomers without any overlap, unlike the partial overlap reported in three-body coincidence studies [50, 52, 53]. In Fig. 4(d), we further incorporate the angle between two  $C^+$  ions  $\theta_{34} = \angle(C^+, C^+)$  — the second-strongest discriminator — to make a two-dimensional angle correlation plot. This plot reveals two distinct islands corresponding to the *cis* and *trans* isomers. These well separated regions demonstrate that relative fragment orientations encode key molecular characteristics and reinforce the effectiveness of these angles in differentiating structural isomers.

By leveraging ML models such as Random Forest, we can systematically identify the most informative observables for Coulomb explosion imaging studies. This approach not only enhances our ability to classify isomers but also provides a framework for feature selection in fu-

ture studies of polyatomic molecular fragmentation.

We now extend our analysis to include four distinct molecular geometries: *cis*-DCE, *trans*-DCE, the *twisted* 1,2-DCE intermediate geometry, and 1,1-DCE. Their ball-and-stick models are illustrated in Fig. 5(a). The *twisted* geometry represents a midpoint in the torsional transition between *cis* and *trans* configurations, while 1,1-DCE represents a structure where hydrogen and chlorine migrations are involved (similar to acetylene-vinylidene isomerization). Together, these geometries offer a broader perspective on conformational changes that may occur in photoinduced reaction dynamics that would be desirable to identify in a time-dependent pump-probe experiment. It is important to note that the following analysis is based on simulated data, as experimental results are not available for the transient *twisted* 1,2-DCE and 1,1-DCE. Given that our simulations closely reproduce the experimental data presented earlier, we believe that this analysis is well justified and provides meaningful insights into the structural dynamics under investigation.

We will apply both unsupervised learning (i.e., clustering) and supervised learning (i.e., classification) techniques to systematically analyze the momentum-space signatures of the isomers. Figure 5(a) presents the clustering results obtained through dimensionality reduction using UMAP, where all molecular configurations clearly separate into distinct clusters. These clusters can be accurately identified by HDBSCAN. This result shows that far more detailed structural differences from CEI data can be encoded in a reduced representation.

Since the *twisted* geometry is nonplanar, the dihedral angle needs to be included to distinguish these structures in real space. We mimic the effect of this quantity in the fragment momentum space by introducing a higher-order correlation — angles between planes:  $\phi_{ijkl}$  — as a structural descriptor.  $\phi_{ijkl}$  is calculated from four momentum vectors where each pair —  $(\vec{p}_i, \vec{p}_j)$  and  $(\vec{p}_k, \vec{p}_l)$  — defines a plane. The discriminative power analysis shown in Fig. 5(b) shows that  $\theta_{56} = \angle(Cl^+, Cl^+)$  and  $\theta_{12} = \angle(H^+, H^+)$  are still among the most important discriminators.

Fig. 5(c) shows that the 1D distribution of  $\theta_{56}$  can reveal partial separation between isomers but cannot be used as a single feature to distinguish all the isomer structures. Significant overlap persists, particularly among the *twisted* and 1,1-DCE structures, demonstrating that this observable alone does not efficiently capture the difference between *cis-trans* isomerization and other processes.

The two-dimensional correlation between  $\theta_{56}$  and  $\theta_{12}$ , as shown in Fig. 5(d), slightly enhances the separation, eliminating minor overlap and cleanly resolving *cis* and *trans* from the other two (i.e., *twisted* and 1,1-DCE). However, complete differentiation of all structures requires additional dimensions. A natural question arises: which feature is most effective for differentiating *twisted*-1,2-DCE and 1,1-DCE structures? As expected,  $\phi_{1256}$  — the angle between two planes formed by protons and

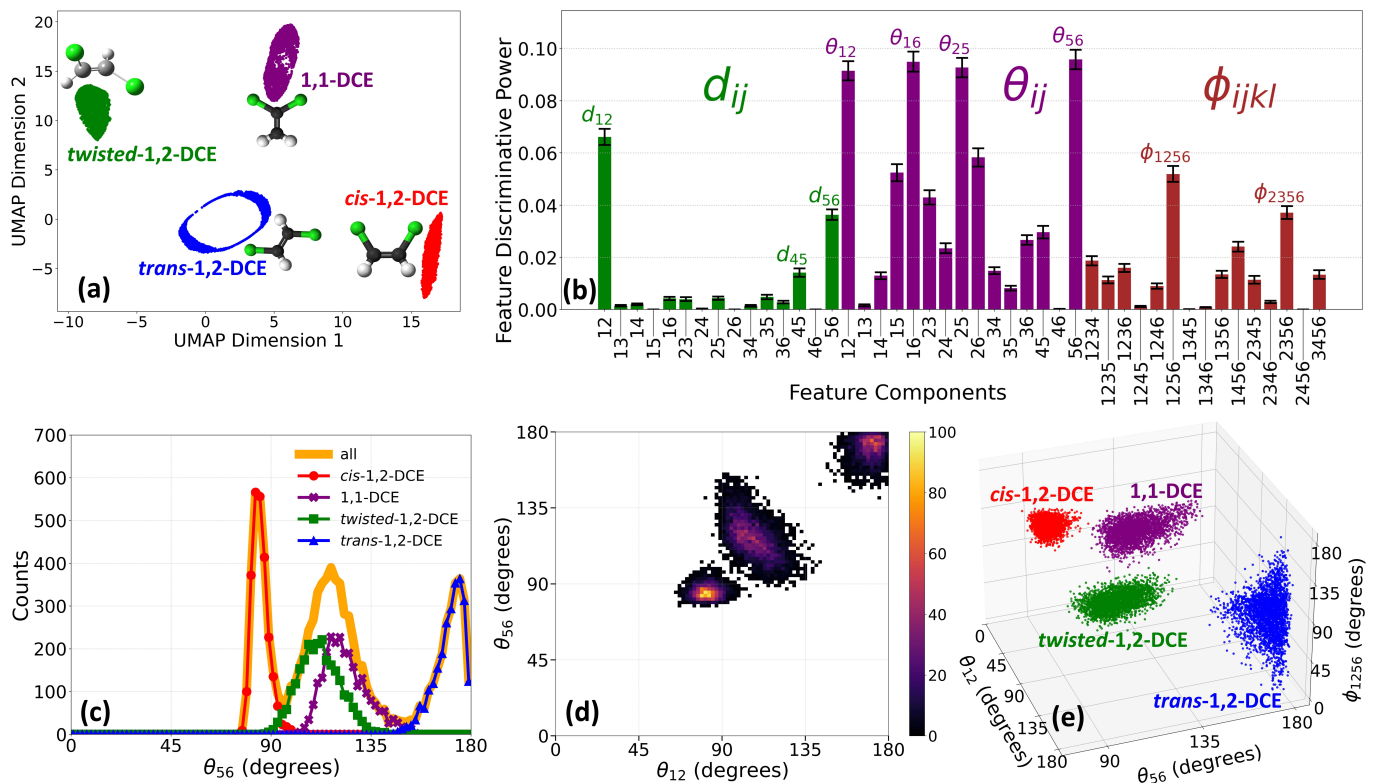


FIG. 5. Multidimensional analysis for structure differentiation. (a) Dimensional reduction and clustering analysis of a mixture of four isomers — *cis*-, *trans*-, *twisted*-1,2-DCE, and 1,1-DCE — where *ball-and-stick* models of these isomers are also illustrated. (b) Discriminative power analysis of features constructed using higher-order correlations between momentum vectors, categorized into modulus difference (green) and angle (purple) between two momentum vectors, and angle between two planes (brown) formed by four momentum vectors. (c-e) demonstrate the effectiveness of high-dimensional data in differentiating isomers, where the separation between these structures is improved sequentially from one- to two- and three-dimensions.

chlorine ions — is the most critical discriminator, which can clearly separate the two (SI, Fig. S17). This can be quantified by performing a similar analysis to Fig. 5(b), restricted to only these two structures (SI, Fig. S18).

Fig. 5(e) shows a 3D representation incorporating  $\phi_{1256}$  in addition to  $\theta_{56}$  and  $\theta_{12}$ . This visualization reveals four distinct clusters and underscores the necessity of leveraging multiple observables to achieve a clear separation of similar molecular structures. In principle, additional dimensions can be incorporated if needed.

Overall, these findings reinforce the key insight that measurement with low-dimensional data is insufficient for robust classification and highlight the advantages of the high-dimensional data provided by multi-coincident CEI. Furthermore, it is not a priori clear which observables will be most important, and the ML techniques presented here provide an automatic way of determining these quickly. Notably, this analysis does not require differentiation between ions of the same element, simplifying its practical implementation in experiments. In principle, CEI data can also be further exploited to distinguish these seemingly identical ions (of the same element), an interesting topic to be explored in a future publication.

To test the limits of the dimensionality reduction approach, we explore next how a large spread of possible product geometries will affect the ability to differentiate between structures. Photoexcitation deposits substantial energy into the molecules. This additional energy can broaden their spatial and kinetic energy distributions, thereby widening the final fragment-momentum spread relative to ground-state isomers. Fig. 6(a) shows the simulated six-body momentum map for the ( $H^+$ ,  $H^+$ ,  $C^+$ ,  $C^+$ ,  $Cl^+$ ,  $Cl^+$ ) channel of a mixture of *cis*-, *trans*-, *twisted*-1,2-DCE, and 1,1-DCE mimicking such scenario. In this simulation, the parameters for spatial deviation and kinetic energy are 0.25 Å and 500 meV for *cis*- and *trans*-1,2-DCE (same as before), and 0.5 Å and 3 eV for *twisted*-1,2-DCE and 1,1-DCE. As expected, the momentum distribution is very broad and without any visually distinctive features that could be assigned by eye to a particular geometry. Reducing the high-dimensional data to 2D using unsupervised UMAP as before [Fig. 6(b)] results in partially overlapping clouds with less pronounced separation between different geometries (especially between *cis*-1,2-DCE and 1,1-DCE isomers). In this situation, one can consider looking at fragmentation channels with higher final charge states (if avail-

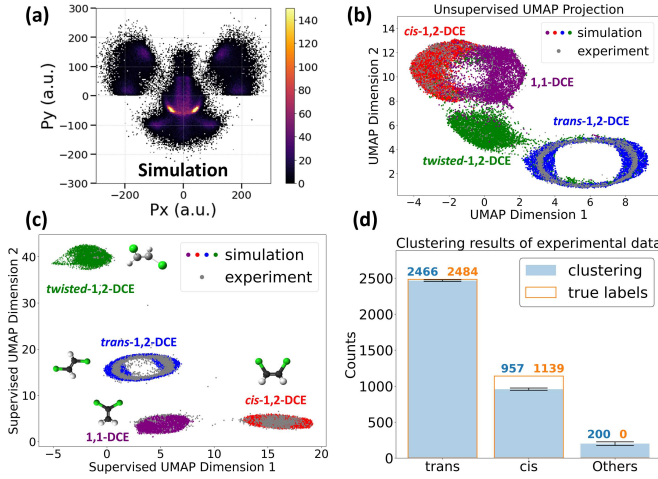


FIG. 6. Supervised UMAP classification of experimental CEI data. (a) Simulated momentum map for the six-body fragmentation channel ( $H^+$ ,  $H^+$ ,  $C^+$ ,  $C^+$ ,  $Cl^+$ ,  $Cl^+$ ) arising from a mixture of *cis*-, *trans*-, *twisted*-1,2-DCE, and 1,1-DCE. (b) Unsupervised two-dimensional UMAP projection of the simulated events (colour-coded by isomer) results in partial overlap between geometries. (c) Supervised UMAP embedding trained exclusively on the simulated labels. Experimental events (gray) are projected into the same latent space and overlap almost perfectly with their respective simulation clusters. (d) Recovery of molecular identity from the experimental data in the supervised space. Filled bars: assignment based on clustering analysis (with error bars originated from the stochastic nature of UMAP are shown in black); outlined bars: ground-truth labels derived independently. Numbers above the bars denote assigned (left) and true (right) counts.

able), which increases the separation (SI, Sec. IV D). On the other hand, one can also use the simulated data to guide the experimental analysis. The idea is to simulate CEI of a few key geometries and perform data reduction, creating a 2D map of structures for guiding experimental analysis. Experimental data of *cis*- and *trans*-1,2-DCE (gray) plotted on the same coordinates show very good overlap with their respective simulation clusters (colored by true labels). However, since the separation between geometries is not sufficiently distinct, automatic clustering is difficult. To overcome this, one can train a supervised UMAP embedding on the labeled simulated data to obtain better separation for automatic clustering analysis. The algorithm optimizes two non-linear combinations of the original momentum components that maximize the separation between the four geometries, producing a 2D latent space that cleanly resolves four well-separated clusters [Fig. 6(c)]. Projecting the experimental data of *cis*- and *trans*-1,2-DCE into this simulation-trained latent space (gray) shows near-perfect overlap with their respective simulation clusters. This excellent agreement validates the feasibility of this approach, showing that supervised machine learning on pure simulation can serve as an appropriate guide for experimental data analysis. Finally, simple density-based

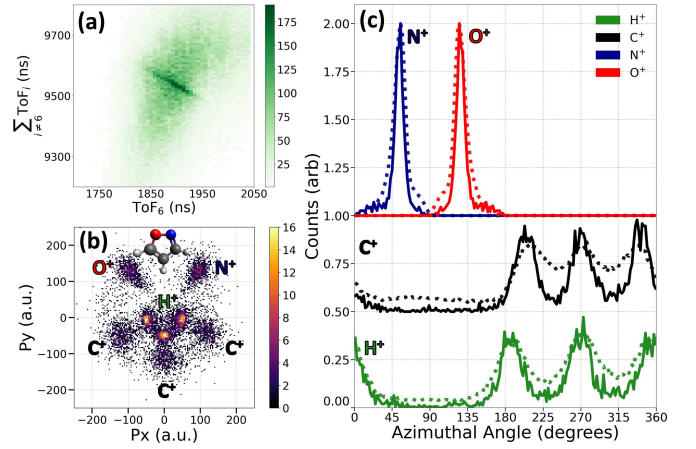


FIG. 7. (a) Photoion coincidence map corresponding to the eight-body fragmentation channel ( $H^+$ ,  $H^+$ ,  $H^+$ ,  $C^+$ ,  $C^+$ ,  $C^+$ ,  $N^+$ ,  $O^+$ ) of isoxazole. The coincidence ion yield is plotted as a function of the ToF of fragment 6 and the total ToF of all other ions. (b) Newton map of the eight-body complete coincidence Coulomb explosion channel. The molecular plane is defined with the vector difference between  $N^+$  and  $O^+$  along the  $p_x$  axis and their vector sum in the upper  $p_x p_y$  plane. The inset shows a ball-and-stick model of the isoxazole molecule. (c) Distributions of the azimuthal angle for the fragment ions in the molecular plane. Solid curves represent the eight-body complete coincidence channel while the dotted curves correspond to the four-fold ( $H^+$ ,  $C^+$ ,  $N^+$ ,  $O^+$ ) partial coincidence channel. The distribution of  $C^+$  is shifted up by 0.5, and  $N^+$  and  $O^+$  by 1.0 for clarity.

clustering (HDBSCAN) of the experimental data in this supervised space recovers  $\approx 99\%$  of trans and  $\approx 84\%$  of cis events, with an overall misclassification rate of just 5.5% [Fig. 6(d)]. Comparable metrics are obtained when the simulation parameters are varied over physically reasonable ranges (SI, Sec. IV C), indicating that the results are robust to uncertainties in the details of the simulation. These results also show that our model can generalize well to real data. We attribute this high performance to two main factors: first is the “complete” CEI mode, which encodes very rich structural information, and second is the ability of UMAP in preserving both global (large-scale changes between different isomers) and local (small-scale variation of each isomer) structures. The unique combination of these two techniques makes the identification of molecular structures very robust. It is worth noting that, in many cases, there is no linear combination of the original momentum components that can produce a comparable separation of all four geometries, making conventional analysis virtually impossible to achieve the results demonstrated here (SI, Sec. IV C). In contrast, our supervised UMAP approach cleanly resolves all geometries and transfers seamlessly to real data, opening the door to monitoring complex dynamical transformation of molecular structures in pump-probe studies of polyatomic molecules.

With currently available tabletop laser and detector technology, it is possible to achieve more than six-ion coincidence. As demonstrated in Fig. 7, we can break all the chemical bonds and completely dissociate isoxazole ( $\text{C}_3\text{H}_3\text{NO}$ ) into atomic ions and detect all these ions in the eight-body fragmentation channel ( $\text{H}^+, \text{H}^+, \text{H}^+, \text{C}^+, \text{C}^+, \text{C}^+, \text{N}^+, \text{O}^+$ ). Momentum conservation, manifesting in a diagonal lines with negative slope, is indicated in the coincidence map in Fig. 7(a), and the corresponding CEI pattern is shown in Fig. 7(b). Previously, we have used a subset of four ions ( $\text{H}^+, \text{C}^+, \text{N}^+, \text{O}^+$ ) in coincidence to create a similar image of this molecule [14]. Fig. 7(c) compares the distributions of azimuthal angles for the ions from the complete eight-body (solid) and the partial four-fold (dotted) coincidences. Their main features are in good agreement, similar to the results on DCE, but the complete coincidence channel shows narrower distributions, and its background-free nature can be seen, for example, in the zero baseline of the  $\text{C}^+$  and  $\text{H}^+$  distributions, which can be exploited to characterize contributions from weak channels and minority species. This example of eight-fold coincidence highlights the potential applications of the presented method to a broad range of molecular systems.

In conclusion, our work demonstrates the power of “complete” CEI—where all atomic ions are detected in coincidence—in providing background-free, detailed structural information of isolated, intermediate-sized polyatomic molecules on a shot-by-shot basis. We show that such complete coincident measurement of up to eight ionic fragments is feasible with regular tabletop laser sources. This capability opens the door to follow the time-dependent motion of all the atoms during molecular structural transformation in photoinduced chemical reactions at the single-molecule level. In order to fully exploit the rich information embedded in multi-coincidence Coulomb explosion patterns, we introduce an automatic, scalable ML-based analysis framework, providing a powerful approach for identifying subtle structural variations, which was successfully demonstrated on dichloroethylene.

The method demonstrated here can facilitate the investigations of other dynamics, such as ultrafast proton transfer [61], fragmentation [62], and symmetry-breaking [63] dynamics in dimers of triatomic molecules (six atoms) or intermediate-sized molecules (up to eight atoms) with unprecedented structural insights. This framework naturally extends to larger polyatomic molecules [14, 17, 19, 32] and can further accommodate conformers, chiral molecules, and molecular dimers, where multidimensional CEI combined with ML can help resolve subtle differences in fragmentation patterns between coexisting configurations. While “complete” CEI with six- and eight-ion coincidences reported in this work represents a substantial advancement compared to previous work, we anticipate a feasible extension to even higher-fold coincidence measurements for larger molecu-

lar systems in the near future by leveraging several experimental developments, including higher-repetition-rate and intense light sources (such as kilohertz-to-megahertz intense light sources), advanced detector technologies, and improved data analysis pipelines [19, 64, 65] (a comprehensive discussion is provided in Sec. I of the SI). Recent work has proposed clustering algorithms as a potential tool for distinguishing structurally similar proteins based on simulated average explosion footprints [66]. While our current work focuses on CEI, a similar ML approach can be extended to data produced by other experimental or theoretical techniques. The continued integration of advanced data science techniques into CEI and other methods will thus pave the way for more detailed and accurate imaging of molecular structures and their dynamic transformations [67–69].

## METHODS

### Experimental details

The experimental setup, shown in Fig. 8, has been described in detail elsewhere [14]. Briefly, a Ti:sapphire laser system (Coherent Legend Elite Duo) operating at 3 kHz delivered 25-fs near-infrared pulses centered at 810 nm. The laser power was controlled using a zero-order half-wave plate and a thin-film polarizer. The pulses were focused into the interaction region of a double-sided velocity map imaging (VMI) spectrometer using a 75-mm focal-length concave mirror, reaching a peak intensity of approximately  $10^{15}$  W/cm<sup>2</sup>.

The molecular samples—*cis*- and *trans*-1,2-DCE (*cis*:  $\geq 99\%$ , Sigma-Aldrich D62209; *trans*:  $\geq 98\%$ , Sigma-Aldrich D62004)—were used without further purification. Due to their relatively high vapor pressures at room temperature, no heating or carrier gas was required. The sample container was connected to a stainless steel gas manifold and went through multiple freeze-pump-thaw cycles to remove air and dissolved gases. Finally, the sample vapor was expanded into vacuum through a 30- $\mu\text{m}$  nozzle into the jet chamber. A 500- $\mu\text{m}$  skimmer was placed a few millimeters downstream (in the zone of silence) to select the center of the expanding molecular beam before delivering it toward the interaction region after another differential pumping stage.

Ionic fragments, produced by the interaction between the samples and the laser, are directed towards the detector using a series of electrostatic lenses, with typical voltages shown in Fig. 9. The detector consisted of a set of 80 mm diameter microchannel plates (MCPs)—a funnel plate in front and a standard back plate—followed by a delay-line position-sensitive quad-anode (Roentdek DLD80). The funnel MCP significantly enhances the detection efficiency by widening the input area with funnel-shaped microchannels [37]. The amplified MCP and delay-line signals were processed using a constant fraction discriminator (CFD) and then recorded with a multi-



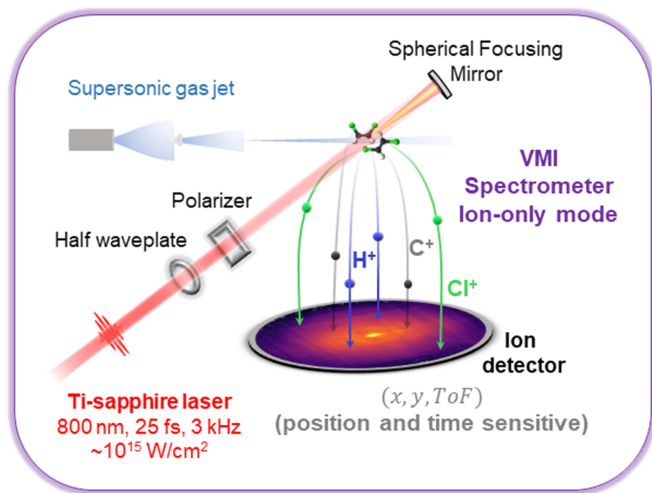


FIG. 8. Schematic of the experimental setup used for laser-induced Coulomb explosion imaging. A Ti:sapphire laser (810 nm, 25 fs, 3 kHz,  $\sim 10^{15}$  W/cm<sup>2</sup>) is focused into a cold molecular beam produced by supersonic expansion. The laser beam is directed into the interaction region using a spherical focusing mirror. Fragment ions are guided toward the detector by electrostatic fields from a double-sided velocity-map imaging (VMI) spectrometer operating in ion-only mode. The detector records the time-of-flight and impact position of all detected ions for each laser shot. This allows for coincidence detection on an event-by-event basis and enables reconstruction of the three-dimensional momenta of the fragment ions.

hit time-to-digital converter (TDC). This setup enabled event-by-event detection of multiple coincident ions from each laser shot, similar to a COLTRIMS apparatus. For every detected ion, the time-of-flight and impact position were recorded, allowing full three-dimensional momentum reconstruction for each fragment.

In this study, we only analyzed events where all the ionic fragments were detected and discarded the rest. Specifically, we only analyzed events where we detected at least two H<sup>+</sup>, two C<sup>+</sup> and two Cl<sup>+</sup> ions for C<sub>2</sub>H<sub>2</sub>Cl<sub>2</sub> (6-fold coincidence) and three H<sup>+</sup>, three C<sup>+</sup>, one N<sup>+</sup> and one O<sup>+</sup> ions for C<sub>3</sub>H<sub>3</sub>NO (8-fold coincidence). This was ensured by gating on the corresponding regions in the recorded ion time-of-flight mass spectrum and then applying momentum conservation constraints to reject false coincidence events, i.e., those cases where the detected ions originated from more than one molecule. After this filtering, the laboratory-frame data of the channel of interest is rotated into the recoil frame (molecular frame) as described in the main text, which allows for better data visualization and simplifies further processing since it eliminates translations and rotations from the data.

The “complete” coincidence events selected as described above constitute only a small fraction of the total measured data set. The vast majority are “incomplete” events, where one or more ions were not detected due to the finite detection efficiency, or events where the molecule did not fully atomize into singly charged atomic

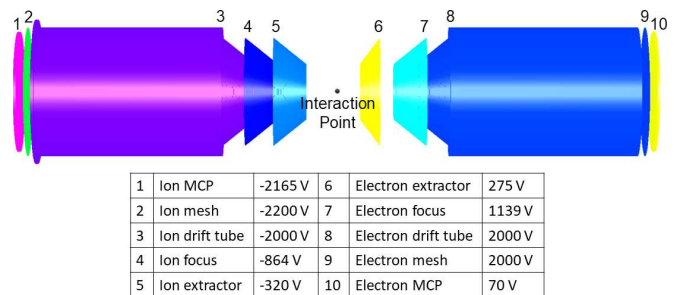


FIG. 9. Schematic of the double-sided velocity-map imaging (VMI) spectrometer and the electrostatic voltages applied to each element during the experiment. The interaction region is centered between the ion-side (left) and electron-side (right) electrodes. Only the ion signals were recorded in this experiment. The voltages shown represent typical operating conditions and are listed next to their corresponding labeled elements.

fragments. Our data also contains other “complete” CEI fragmentation channels (SI, Fig. S4), which could potentially be used to obtain a more complete picture of the molecule and its dynamics.

### Coulomb explosion simulation

Our classical Coulomb explosion simulations start with optimizing the geometry of each molecule in its neutral electronic ground state at the B3LYP/aug-cc-pVDZ level. The resulting structures are reported in Sec. III A of the SI. From this equilibrium geometry, we generated the initial condition by varying the spatial position of each atom within a Gaussian distribution of 0.25 Å standard deviation and further adding a total kinetic energy of 500 meV (randomly partitioned among the atoms), unless otherwise stated. These parameters were chosen empirically to closely reproduce the widths of the experimentally observed momentum distributions (as shown in Fig. 1 and Fig. 2). Although broader than the more physically meaningful Wigner distributions [14, 38], this approach better captures additional broadening effects intrinsic to the Coulomb explosion process. These effects include nuclear motion during ionization, kinetic energy imparted by the laser field, and contributions from multiple ionic states, which are very challenging to compute with a fully quantum mechanical model, even for very small molecules. Our simulation agrees much better with the experimental data compared to starting with a Wigner distribution, as shown in Fig. S5. For statistical significance, we sample 20,000 initial geometries per molecule. We then perform classical Coulomb explosion simulations on the sampled geometries by numerically solving coupled Newton’s equations of motion, where each atom is modeled as a point charge. Our simulations assume instantaneous vertical ionization leading directly to point charges, where each atom obtains its final charge upon ionization. It also assumes that the re-

pulsive potential of the highly charged cations leading to multibody fragmentations is purely Coulombic and that the molecule fragments completely into charged atomic ions without any internal energy.

Our simulation is equivalent to a classical molecular dynamics simulation where the force field is set as purely Coulombic interaction between point charges. The simulation is tailored specifically to the fragmentation channel of interest that we chose to investigate by filtering our coincidence data. This approach differs from more generic simulations, which aim to statistically model the distribution of multiple charge states and fragmentation pathways. Our method is thus computationally lighter and more focused, made possible by the ability to select and analyze specific channels through the “complete” coincidence detection technique.

Despite its simplicity, our Coulombic model effectively reproduces key experimental features because Coulomb repulsion significantly dominates chemical bond interactions at high-charge states in determining the fragmentation dynamics. Comparisons with a more sophisticated model using XMDYN (as demonstrated by Boll *et al.* [17]) show that although both models somewhat overestimate the magnitudes of fragment momenta, they accurately reproduce angle correlations between fragment momenta. Similar trends are consistently observed across various molecular systems in both laser-based and XFEL-based experiments [14, 17, 38], suggesting that for high charge states, the Coulomb force indeed dominates over other interactions. Thus, the simplicity of our model does not compromise the accuracy needed for clustering analyses, particularly when comparing between molecules, where the angle correlation between momentum vectors is important rather than the overall absolute magnitudes. Furthermore, unlike previously demonstrated models [14, 17, 38] that yield overly narrow momentum distributions compared to experimental results—limiting their effectiveness in realistic clustering demonstrations—our modified model produces broader, experimentally realistic distributions (see SI, Fig. S5). This broadening significantly enhances the practical relevance and applicability of our clustering analysis.

### Machine-learning-based analysis in Python

To analyze high-dimensional momentum-space data from multi-coincidence CEI, we employed a combination of unsupervised and supervised machine learning methods for different purposes as listed below.

- Dimensionality reduction (unsupervised): UMAP [56], Principal Component Analysis (PCA), t-distributed Stochastic Neighbor Embedding (t-SNE) [70]
- Clustering (unsupervised): HDBSCAN [57]
- Dimensional optimization (supervised): supervised UMAP, Linear Discriminant Analysis (LDA) [71]

- Feature importance ranking (supervised): Random Forest Classifier [58]

Among these techniques, UMAP (unsupervised and supervised), HDBSCAN, and Random Forest Classifier were the primary methods discussed in the main text. PCA, t-SNE, LDA are discussed in the SI for a more complete perspective, as these approaches should be used flexibly or combined as appropriate, depending on the dataset and objective. In Sec. IV A, we compared the performance of different data reduction techniques on identical inputs, quantitatively quantified by computing the Silhouette Score [72] and Davies-Bouldin Index [73] for each method (more explanations in the SI). In this study, we found that UMAP consistently outperformed other methods.

Because UMAP is inherently stochastic, repeated runs on the same dataset may yield slightly different results. In SI, Sec. IV B, we evaluated the stability of our data reduction using UMAP and confirmed that the results are highly stable.

HDBSCAN was implemented using the `hdbscan` package [74] and used as an unsupervised clustering algorithm that identifies groups of points based on variations in local point density, without requiring the number of clusters to be specified in advance. It constructs a hierarchy of clusters using density-based connectivity, and then condenses this hierarchy to extract a flat clustering that balances stability and detail. This method was particularly effective in identifying distinct clusters in the reduced momentum-space representations of isomeric structures.

To perform supervised classification and feature importance ranking (relative discriminative power analysis), we used Random Forest Classifier from `scikit-learn` [75]. This ensemble method constructs a collection of decision trees using bootstrapped samples, selecting random feature subsets at each split to improve generalization. The model was trained on labeled events, and feature importance was derived from how much each feature contributed to reducing classification uncertainty of molecular structural patterns across the ensemble of decision trees. Similar to UMAP, Random Forests are stochastic due to their initialization with pseudorandom seeds; results can vary slightly between runs. To mitigate this, we repeated the classification 100 times with different random states and reported the mean and standard deviation of the relative discriminative power.

All computations were performed on standard scientific computing hardware using free and open-source software: Python (version 3.12.3), `scikit-learn` (version 1.6.1), `umap-learn` (version 0.5.7), and `hdbscan` (version 0.8.39).

### DATA AVAILABILITY

The data generated in this study are provided in Source Data files. Further data is available from the cor-

responding author upon reasonable request.

## CODE AVAILABILITY

Experimental data is collected using VMUSBReadout (open source, available at <https://sourceforge.net/projects/nscldaq/>). All machine learning analyses were performed using free and open-source software: Python (version 3.12.3; <https://www.python.org/>), scikit-learn (version 1.6.1; <https://scikit-learn.org/>), umap-learn (version 0.5.7; <https://umap-learn.readthedocs.io/>), and hdbscan (version 0.8.39; <https://hdbscan.readthedocs.io/>). The Coulomb explosion simulation code is available at <https://doi.org/10.5281/zenodo.16815021>.

## ACKNOWLEDGMENTS

We thank Van-Hung Hoang for many useful discussions on the simulation. We are grateful to the technical

staff of the J.R. Macdonald Laboratory for their support. This work and the operation of the J.R. Macdonald Laboratory are supported by the Chemical Sciences, Geosciences, and Biosciences Division, Office of Basic Energy Sciences, Office of Science, U.S. Department of Energy, Grant no. DE-FG02-86ER13491. The machine learning aspect of this work was supported by a GRIPex award from Kansas State University. A.V. is supported by the National Science Foundation Grant no. PHYS-2409365.

## AUTHOR CONTRIBUTIONS

H.V.S.L. and D.R. conceptualized the study. A.S.V. and H.V.S.L. conducted the experiment, carried out Coulomb explosion simulations, performed machine learning analysis, and analyzed the data. H.V.S.L. and A.S.V. interpreted the results in discussion with input from all authors. A.S.V. and H.V.S.L. produced the figures and drafted the initial manuscript. A.S.V., H.V.S.L., L.G., D.R., and A.R. contributed to iterative discussions and revisions of the final manuscript.

- 
- [1] A. H. Zewail, Femtochemistry: Atomic-Scale Dynamics of the Chemical Bond, *The Journal of Physical Chemistry A* **104**, 5660 (2000).
  - [2] S. P. Weathersby, G. Brown, M. Centurion, T. F. Chase, R. Coffee, J. Corbett, J. P. Eichner, J. C. Frisch, A. R. Fry, M. Gühr, N. Hartmann, C. Hast, R. Hetzel, R. K. Jobe, E. N. Jongewaard, J. R. Lewandowski, R. K. Li, A. M. Lindenberg, I. Makasyuk, J. E. May, D. McCormick, M. N. Nguyen, A. H. Reid, X. Shen, K. Sokolowski-Tinten, T. Vecchione, S. L. Vetter, J. Wu, J. Yang, H. A. Dürr, and X. J. Wang, Mega-electron-volt ultrafast electron diffraction at SLAC National Accelerator Laboratory, *Review of Scientific Instruments* **86**, 073702 (2015).
  - [3] M. P. Minitti, J. M. Budarz, A. Kirrander, J. S. Robinson, D. Ratner, T. J. Lane, D. Zhu, J. M. Glowina, M. Kozina, H. T. Lemke, M. Sikorski, Y. Feng, S. Nelson, K. Saita, B. Stankus, T. Northey, J. B. Hastings, and P. M. Weber, Imaging Molecular Motion: Femtosecond X-Ray Scattering of an Electrocyclic Chemical Reaction, *Phys. Rev. Lett.* **114**, 255501 (2015).
  - [4] A. A. Ischenko, P. M. Weber, and R. J. D. Miller, Capturing Chemistry in Action with Electrons: Realization of Atomically Resolved Reaction Dynamics, *Chemical Reviews* **117**, 11066 (2017).
  - [5] J. M. Ruddock, H. Yong, B. Stankus, W. Du, N. Goff, Y. Chang, A. Odate, A. M. Carrascosa, D. Bellshaw, N. Zotev, M. Liang, S. Carbajo, J. Koglin, J. S. Robinson, S. Boutet, A. Kirrander, M. P. Minitti, and P. M. Weber, A deep UV trigger for ground-state ring-opening dynamics of 1,3-cyclohexadiene, *Science Advances* **5**, eaax6625 (2019).
  - [6] Y. Liu, S. L. Horton, J. Yang, J. P. F. Nunes, X. Shen, T. J. A. Wolf, R. Forbes, C. Cheng, B. Moore, M. Centurion, K. Hegazy, R. Li, M.-F. Lin, A. Stolow, P. Hockett, T. Rozgonyi, P. Marquetand, X. Wang, and T. Weinacht, Spectroscopic and structural probing of excited-state molecular dynamics with time-resolved photoelectron spectroscopy and ultrafast electron diffraction, *Phys. Rev. X* **10**, 021016 (2020).
  - [7] M. Zhang, Z. Guo, X. Mi, Z. Li, and Y. Liu, Ultrafast Imaging of Molecular Dynamics Using Ultrafast Low-Frequency Lasers, X-ray Free Electron Lasers, and Electron Pulses, *J. Phys. Chem. Lett.* **13**, 1668 (2022).
  - [8] D. Filippetto, P. Musumeci, R. K. Li, B. J. Siwick, M. R. Otto, M. Centurion, and J. P. F. Nunes, Ultrafast electron diffraction: Visualizing dynamic states of matter, *Rev. Mod. Phys.* **94**, 045004 (2022).
  - [9] Z. Vager, R. Naaman, and E. P. Kanter, Coulomb explosion imaging of small molecules, *Science* **244**, 426 (1989).
  - [10] H. Stapelfeldt, E. Constant, and P. B. Corkum, Wave packet structure and dynamics measured by coulomb explosion, *Physical Review Letters* **74**, 3780 (1995).
  - [11] H. Hasegawa, A. Hishikawa, and K. Yamanouchi, Coincidence imaging of coulomb explosion of CS<sub>2</sub> in intense laser fields, *Chemical Physics Letters* **349**, 57 (2001).
  - [12] M. Pitzer, M. Kunitski, A. S. Johnson, T. Jahnke, H. Sann, F. Sturm, L. P. H. Schmidt, H. Schmidt-Böcking, R. Dörner, J. Stohner, J. Kiedrowski, M. Reggelin, S. Marquardt, A. Schießer, R. Berger, and M. S. Schöffler, Direct determination of absolute molecular stereochemistry in gas phase by coulomb explosion imaging, *Science* **341**, 1096 (2013).
  - [13] H. V. S. Lam, S. Yarlagadda, A. Venkatachalam, T. N. Wangjam, R. K. Kushawaha, C. Cheng, P. Svihira, A. Nomerotski, T. Weinacht, D. Rolles, and V. Kumarapapan, Angle-dependent strong-field ionization and fragmentation of carbon dioxide measured using rotational wave packets, *Physical Review A* **102**, 043119 (2020).

- [14] H. V. S. Lam, A. S. Venkatachalam, S. Bhattacharyya, K. Chen, K. Borne, E. Wang, R. Boll, T. Jahnke, V. Kumarappan, A. Rudenko, and D. Rolles, Differentiating Three-Dimensional Molecular Structures Using Laser-Induced Coulomb Explosion Imaging, *Phys. Rev. Lett.* **132**, 123201 (2024).
- [15] H. V. S. Lam, V.-H. Hoang, A. S. Venkatachalam, S. Bhattacharyya, K. Chen, S. Jacob, S. Kudagama, T. T. Nguyen, D. Rolles, U. Thumm, A. Rudenko, and V. Kumarappan, Simultaneous imaging of vibrational, rotational, and electronic wave-packet dynamics in a triatomic molecule, *Phys. Rev. A* **111**, L061101 (2025).
- [16] E. Kukk, K. Motomura, H. Fukuzawa, K. Nagaya, and K. Ueda, Molecular dynamics of xfel-induced photodissociation, revealed by ion-ion coincidence measurements, *Applied Sciences* **7**, 10.3390/app7050531 (2017).
- [17] R. Boll, J. M. Schäfer, B. Richard, K. Fehre, G. Kastirke, Z. Jurek, M. S. Schöffler, M. M. Abdullah, N. Anders, T. M. Baumann, S. Eckart, B. Erk, A. D. Fanis, R. Dörner, S. Grundmann, P. Grychtol, A. Hartung, M. Hofmann, M. Ilchen, L. Inhester, C. Janke, R. Jin, M. Kircher, K. Kubicek, M. Kunitski, X. Li, T. Mazza, S. Meister, N. Melzer, J. Montano, V. Music, G. Nalin, Y. Ovcharenko, C. Passow, A. Pier, N. Rennhack, J. Rist, D. E. Rivas, D. Rolles, I. Schlichting, L. P. H. Schmidt, P. Schmidt, J. Siebert, N. Strenger, D. Trabert, F. Trinter, I. Vela-Perez, R. Wagner, P. Walter, M. Weller, P. Ziolkowski, S.-K. Son, A. Rudenko, M. Meyer, R. Santra, and T. Jahnke, X-ray multiphoton-induced coulomb explosion images complex single molecules, *Nature Physics* **18**, 423 (2022).
- [18] T. Jahnke, S. Mai, S. Bhattacharyya, K. Chen, R. Boll, M. E. Castellani, S. Dold, U. Frühling, A. E. Green, M. Ilchen, R. Ingle, G. Kastirke, H. V. S. Lam, F. Lever, D. Mayer, T. Mazza, T. Mullins, Y. Ovcharenko, B. Senftleben, F. Trinter, Atia-Tul-Noor, S. Usenko, A. S. Venkatachalam, A. Rudenko, D. Rolles, M. Meyer, H. Ibrahim, and M. Gühr, Direct observation of ultrafast symmetry reduction during internal conversion of 2-thiouracil using coulomb explosion imaging, *Nature Communications* **16**, 2074 (2025).
- [19] B. Richard, R. Boll, S. Banerjee, J. M. Schäfer, Z. Jurek, G. Kastirke, K. Fehre, M. S. Schöffler, N. Anders, T. M. Baumann, S. Eckart, B. Erk, A. De Fanis, R. Dörner, S. Grundmann, P. Grychtol, M. Hofmann, M. Ilchen, M. Kircher, K. Kubicek, M. Kunitski, X. Li, T. Mazza, S. Meister, N. Melzer, J. Montano, V. Music, Y. Ovcharenko, C. Passow, A. Pier, N. Rennhack, J. Rist, D. E. Rivas, D. Rolles, I. Schlichting, L. P. H. Schmidt, P. Schmidt, D. Trabert, F. Trinter, R. Wagner, P. Walter, P. Ziolkowski, A. Rudenko, M. Meyer, R. Santra, L. Inhester, and T. Jahnke, Imaging collective quantum fluctuations of the structure of a complex molecule, *Science* **389**, 650 (2025).
- [20] P. Herwig, K. Zawatzky, M. Grieser, O. Heber, B. Jordon-Thaden, C. Krantz, O. Novotný, R. Repnow, V. Schurig, D. Schwalm, and Z. Vager, Imaging the absolute configuration of a chiral epoxide in the gas phase, *Science* **342**, 1084 (2013).
- [21] A. S. Alnaser, X. M. Tong, T. Osipov, S. Voss, C. M. Maharjan, P. Ranitovic, B. Ulrich, B. Shan, Z. Chang, C. D. Lin, and C. L. Cocke, Routes to control of H<sub>2</sub> coulomb explosion in few-cycle laser pulses, *Physical Review Letters* **93**, 183202 (2004).
- [22] F. Légaré, K. F. Lee, I. V. Litvinyuk, P. W. Dooley, S. S. Wesolowski, P. R. Bunker, P. Dombi, F. Krausz, A. D. Bandrauk, D. M. Villeneuve, and P. B. Corkum, Laser coulomb-explosion imaging of small molecules, *Physical Review A* **71**, 013415 (2005).
- [23] T. Ergler, A. Rudenko, B. Feuerstein, K. Zrost, C. D. Schröter, R. Moshhammer, and J. Ullrich, Spatiotemporal imaging of ultrafast molecular motion: Collapse and revival of the D<sub>2</sub><sup>+</sup> nuclear wave packet, *Physical Review Letters* **97**, 193001 (2006).
- [24] C. Cornaggia, Ultrafast coulomb explosion imaging of molecules, *Laser Physics* **19**, 1660 (2009).
- [25] L. P. H. Schmidt, T. Jahnke, A. Czasch, M. Schöffler, H. Schmidt-Böcking, and R. Dörner, Spatial imaging of the H<sub>2</sub><sup>+</sup> vibrational wave function at the quantum limit, *Phys. Rev. Lett.* **108**, 073202 (2012).
- [26] R. Karimi, W.-K. Liu, and J. Sanderson, Femtosecond laser-induced coulomb explosion imaging, in *Advances in Multi-Photon Processes and Spectroscopy* (World Scientific, 2016) pp. 97–153.
- [27] T. Yatsushashi and N. Nakashima, Multiple ionization and coulomb explosion of molecules, molecular complexes, clusters and solid surfaces, *Journal of Photochemistry and Photobiology C: Photochemistry Reviews* **34**, 52 (2018).
- [28] A. Hishikawa, A. Matsuda, and M. Fushitani, Ultrafast reaction imaging and control by ultrashort intense laser pulses, *Bulletin of the Chemical Society of Japan* **93**, 1293 (2020).
- [29] X. Li, X. Yu, P. Ma, X. Zhao, C. Wang, S. Luo, and D. Ding, Ultrafast coulomb explosion imaging of molecules and molecular clusters, *Chinese Physics B* **31**, 103304 (2022).
- [30] T. Severt, Z. L. Streeter, W. Iskandar, K. A. Larsen, A. Gatton, D. Trabert, B. Jochim, B. Griffin, E. G. Champenois, M. M. Brister, D. Reedy, D. Call, R. Strom, A. L. Landers, R. Dörner, J. B. Williams, D. S. Slaughter, R. R. Lucchese, T. Weber, C. W. McCurdy, and I. Ben-Itzhak, Step-by-step state-selective tracking of fragmentation dynamics of water dications by momentum imaging, *Nature Communications* **13**, 5146 (2022).
- [31] A. J. Howard, M. Britton, Z. L. Streeter, C. Cheng, R. Forbes, J. L. Reynolds, F. Allum, G. A. McCracken, I. Gabalski, R. R. Lucchese, C. W. McCurdy, T. Weinacht, and P. H. Bucksbaum, Filming enhanced ionization in an ultrafast triatomic slingshot, *Communications Chemistry* **6**, 81 (2023).
- [32] H. Yuan, Y. Gao, B. Yang, S. Gu, H. Lin, D. Guo, J. Liu, S. Zhang, X. Ma, and S. Xu, Coulomb Explosion Imaging of Complex Molecules Using Highly Charged Ions, *Phys. Rev. Lett.* **133**, 193002 (2024).
- [33] R. Dalitz, On the analysis of  $\tau$ -meson data and the nature of the  $\tau$ -meson, *The London, Edinburgh, and Dublin Philosophical Magazine and Journal of Science* **44**, 1068 (1953).
- [34] J. Rajput, T. Severt, B. Berry, B. Jochim, P. Feizollah, B. Kaderiya, M. Zohrabi, U. Ablikim, F. Ziaee, K. Raju P., D. Rolles, A. Rudenko, K. D. Carnes, B. D. Esry, and I. Ben-Itzhak, Native frames: Disentangling sequential from concerted three-body fragmentation, *Phys. Rev. Lett.* **120**, 103001 (2018).
- [35] T. Severt, J. Rajput, B. Berry, B. Jochim, P. Feizollah, B. Kaderiya, M. Zohrabi, F. Ziaee, K. R. P., D. Rolles, A. Rudenko, K. D. Carnes, B. D. Esry, and I. Ben-Itzhak,



- Native frames: An approach for separating sequential and concerted three-body fragmentation, *Phys. Rev. A* **110**, 053104 (2024).
- [36] E. Wang, S. Bhattacharyya, K. Chen, K. Borne, F. Ziaee, S. Pathak, H. V. S. Lam, A. S. Venkatachalam, X. Chen, R. Boll, T. Jahnke, A. Rudenko, and D. Rolles, Time-resolved coulomb explosion imaging unveils ultrafast ring opening of furan (2023), [arXiv:2311.05099 \[physics.chem-ph\]](https://arxiv.org/abs/2311.05099).
- [37] K. Fehre, D. Trojanowskaja, J. Gatzke, M. Kunitski, F. Trinter, S. Zeller, L. P. H. Schmidt, J. Stohner, R. Berger, A. Czasch, O. Jagutzki, T. Jahnke, R. Dörner, and M. S. Schöffler, Absolute ion detection efficiencies of microchannel plates and funnel microchannel plates for multi-coincidence detection, *Review of Scientific Instruments* **89**, 52 (2018).
- [38] S. Bhattacharyya, K. Borne, F. Ziaee, S. Pathak, E. Wang, A. S. Venkatachalam, X. Li, N. Marshall, K. D. Carnes, C. W. Fehrenbach, T. Severt, I. Ben-Itzhak, A. Rudenko, and D. Rolles, Strong-field-induced coulomb explosion imaging of tribromomethane, *The Journal of Physical Chemistry Letters* **13**, 5845 (2022).
- [39] X. Li, A. Rudenko, M. S. Schöffler, N. Anders, T. M. Baumann, S. Eckart, B. Erk, A. D. Fanis, K. Fehre, R. Dörner, L. Foucar, S. Grundmann, P. Grychtol, A. Hartung, M. Hofmann, M. Ilchen, C. Janke, G. Kastirke, M. Kircher, K. Kubicek, M. Kunitski, T. Mazza, S. Meister, N. Melzer, J. Montano, V. Music, G. Nalin, Y. Ovcharenko, C. Passow, A. Pier, N. Rennhack, J. Rist, D. E. Rivas, I. Schlichting, L. P. H. Schmidt, P. Schmidt, J. Siebert, N. Strenger, D. Trabert, F. Trinter, I. Vela-Perez, R. Wagner, P. Walter, M. Weller, P. Ziolkowski, A. Czasch, D. Rolles, M. Meyer, T. Jahnke, and R. Boll, Coulomb explosion imaging of small polyatomic molecules with ultrashort x-ray pulses, *Physical Review Research* **4**, 013029 (2022).
- [40] X. Li, R. Boll, P. Vindel-Zandbergen, J. González-Vázquez, D. E. Rivas, S. Bhattacharyya, K. Borne, K. Chen, A. De Fanis, B. Erk, R. Forbes, A. E. Green, M. Ilchen, B. Kaderiya, E. Kuk, H. V. S. Lam, T. Mazza, T. Mullins, B. Senfftleben, F. Trinter, S. Usenko, A. S. Venkatachalam, E. Wang, J. P. Cryan, M. Meyer, T. Jahnke, P. J. Ho, D. Rolles, and A. Rudenko, Imaging a light-induced molecular elimination reaction with an X-ray free-electron laser, *Nat Commun* **16**, 7006 (2025).
- [41] T. Endo, S. P. Neville, V. Wanie, S. Beaulieu, C. Qu, J. Deschamps, P. Lassonde, B. E. Schmidt, H. Fujise, M. Fushitani, A. Hishikawa, P. L. Houston, J. M. Bowman, M. S. Schuurman, F. Légaré, and H. Ibrahim, Capturing roaming molecular fragments in real time, *Science* **370**, 1072 (2020).
- [42] T. Eriksson, S. Björkman, and P. Höglund, Clinical pharmacology of thalidomide, *European Journal of Clinical Pharmacology* **57**, 365 (2001).
- [43] S. Habtemariam, Isomerism in organic compounds and drug molecules: Chemistry and significance in biology (The Royal Society of Chemistry, 2023) pp. 149–194.
- [44] D. Patterson, M. Schnell, and J. M. Doyle, Enantiomer-specific detection of chiral molecules via microwave spectroscopy, *Nature* **497**, 475 (2013).
- [45] X. Zhou, Z. Wang, S. Li, X. Rong, J. Bu, Q. Liu, and Z. Ouyang, Differentiating enantiomers by directional rotation of ions in a mass spectrometer, *Science* **383**, 612 (2024).
- [46] J. L. Hansen, J. H. Nielsen, C. B. Madsen, A. T. Lindhardt, M. P. Johansson, T. Skrydstrup, L. B. Madsen, and H. Stapelfeldt, Control and femtosecond time-resolved imaging of torsion in a chiral molecule, *The Journal of Chemical Physics* **136**, 204310 (2012).
- [47] L. Christensen, J. H. Nielsen, C. S. Slater, A. Lauer, M. Brouard, and H. Stapelfeldt, Using laser-induced coulomb explosion of aligned chiral molecules to determine their absolute configuration, *Phys. Rev. A* **92**, 033411 (2015).
- [48] K. Fehre, S. Eckart, M. Kunitski, M. Pitzer, S. Zeller, C. Janke, D. Trabert, J. Rist, M. Weller, A. Hartung, L. P. H. Schmidt, T. Jahnke, R. Berger, R. Dörner, and M. S. Schöffler, Enantioselective fragmentation of an achiral molecule in a strong laser field, *Science Advances* **5**, eaau7923 (2019).
- [49] D. Tsitsionis, F. Trinter, J. B. Williams, K. Fehre, P. V. Demekhin, T. Jahnke, R. Dörner, and M. S. Schöffler, Enantioselective one-photon excitation of formic acid, *Phys. Rev. Lett.* **133**, 093002 (2024).
- [50] U. Ablikim, C. Bomme, H. Xiong, E. Savelyev, R. Obaid, B. Kaderiya, S. Augustin, K. Schnorr, I. Dumitriu, T. Osipov, R. Bilodeau, D. Kilcoyne, V. Kumarappan, A. Rudenko, N. Berrah, and D. Rolles, Identification of absolute geometries of cis and trans molecular isomers by Coulomb Explosion Imaging, *Sci Rep* **6**, 38202 (2016).
- [51] M. Burt, K. Amini, J. W. L. Lee, L. Christiansen, R. R. Johansen, Y. Kobayashi, J. D. Pickering, C. Vallance, M. Brouard, and H. Stapelfeldt, Communication: Gas-phase structural isomer identification by coulomb explosion of aligned molecules, *The Journal of Chemical Physics* **148**, 091102 (2018).
- [52] U. Ablikim, C. Bomme, T. Osipov, H. Xiong, R. Obaid, R. C. Bilodeau, N. G. Kling, I. Dumitriu, S. Augustin, S. Pathak, K. Schnorr, D. Kilcoyne, N. Berrah, and D. Rolles, A coincidence velocity map imaging spectrometer for ions and high-energy electrons to study inner-shell photoionization of gas-phase molecules, *Review of Scientific Instruments* **90**, 055103 (2019).
- [53] J. W. McManus, F. Allum, J. Featherstone, C.-S. Lam, and M. Brouard, Two-Dimensional Projected-Momentum Covariance Mapping for Coulomb Explosion Imaging, *J. Phys. Chem. A* **128**, 3220 (2024).
- [54] S. Pathak, R. Obaid, S. Bhattacharyya, J. Bürger, X. Li, J. Tross, T. Severt, B. Davis, R. C. Bilodeau, C. A. Trallero-Herrero, A. Rudenko, N. Berrah, and D. Rolles, Differentiating and quantifying gas-phase conformational isomers using coulomb explosion imaging, *The Journal of Physical Chemistry Letters* **11**, 10205 (2020).
- [55] H. V. S. Lam, A. S. Venkatachalam, S. Bhattacharyya, E. Wang, K. Borne, K. Chen, A. Rudenko, and D. Rolles, Coulomb explosion imaging: a robust method for distinguishing molecular structures and tracking structural changes in photochemical reactions, in *Ultrafast Non-linear Imaging and Spectroscopy XI*, edited by Z. Liu, D. Psaltis, and K. Shi (SPIE, San Diego, United States, 2023) p. 29.
- [56] L. McInnes, J. Healy, and J. Melville, UMAP: Uniform Manifold Approximation and Projection for Dimension Reduction (2018), [arXiv:1802.03426 \[stat.ML\]](https://arxiv.org/abs/1802.03426).
- [57] R. J. G. B. Campello, D. Moulavi, and J. Sander, Density-Based Clustering Based on Hierarchical Density Estimates, in *Advances in Knowledge Discovery and Data*

- Mining*, edited by J. Pei, V. S. Tseng, L. Cao, H. Motoda, and G. Xu (Springer, Berlin, Heidelberg, 2013) pp. 160–172.
- [58] L. Breiman, Random forests, *Machine Learning* **45**, 5 (2001).
  - [59] H. Stapelfeldt, E. Constant, H. Sakai, and P. B. Corkum, Time-resolved coulomb explosion imaging: A method to measure structure and dynamics of molecular nuclear wave packets, *Physical Review A* **58**, 426 (1998).
  - [60] A. Rudenko, T. Ergler, B. Feuerstein, K. Zrost, C. D. Schröter, R. Moshhammer, and J. Ullrich, Real-time observation of vibrational revival in the fastest molecular system, *Chemical Physics* **329**, 193 (2006).
  - [61] K. Schnorr, M. Belina, S. Augustin, H. Lindenblatt, Y. Liu, S. Meister, T. Pfeifer, G. Schmid, R. Treusch, F. Trost, P. Slavíček, and R. Moshhammer, Direct tracking of ultrafast proton transfer in water dimers, *Science Advances* **9**, eadg7864 (2023).
  - [62] X. Yu, X. Zhang, X. Hu, X. Zhao, D. Ren, X. Li, P. Ma, C. Wang, Y. Wu, S. Luo, and D. Ding, Femtosecond time-resolved neighbor roles in the fragmentation dynamics of molecules in a dimer, *Phys. Rev. Lett.* **129**, 023001 (2022).
  - [63] E. Livshits, D. M. Bittner, F. Trost, S. Meister, H. Lindenblatt, R. Treusch, K. Gope, T. Pfeifer, R. Baer, R. Moshhammer, and D. Strasser, Symmetry-breaking dynamics of a photoionized carbon dioxide dimer, *Nature Communications* **15**, 6322 (2024).
  - [64] P. Walter, M. Holmes, R. Obaid, L. Amores, X. Cheng, J. P. Cryan, J. M. Glowina, X. Li, M.-F. Lin, M. L. Ng, J. Robinson, N. Shivaram, J. Yin, D. Fritz, J. James, J.-C. Castagna, and T. Osipov, The DREAM Endstation at the Linac Coherent Light Source, *Applied Sciences* **12**, 10534 (2022).
  - [65] B. Markovic, C. Bakalis, G. Blaj, X. Defay, D. Doering, A. Gupta, J. Hasi, C. Kenney, P. King, A. Pena-Perez, B. Reese, L. Rota, L. Ruckman, J. Segal, T. Driver, J. Cryan, C. Hansson, and A. Dragone, SparkPix-T: Spatial and Time Resolving Front-End ASIC with MHz-Rate Information Extraction for Momentum Spectroscopy at LCLS-II, in *2023 IEEE Nuclear Science Symposium, Medical Imaging Conference and International Symposium on Room-Temperature Semiconductor Detectors (NSS MIC RTSD)* (2023) pp. 1–1, iSSN: 2577-0829.
  - [66] T. André, I. Dawod, S. Cardoch, E. De Santis, N. m. c. Timneanu, and C. Coleman, Protein structure classification based on x-ray-laser-induced coulomb explosion, *Phys. Rev. Lett.* **134**, 128403 (2025).
  - [67] O. V. Prezhdo, Advancing Physical Chemistry with Machine Learning, *J. Phys. Chem. Lett.* **11**, 9656 (2020).
  - [68] M. W. Dorrity, L. M. Saunders, C. Queitsch, S. Fields, and C. Trapnell, Dimensionality reduction by UMAP to visualize physical and genetic interactions, *Nat Commun* **11**, 1537 (2020).
  - [69] Sheng Ye and Lvshuai Zhu and Zhicheng Zhao and Fan Wu and Zhipeng Li and BinBin Wang and Kai Zhong and Changyin Sun and Shaul Mukamel and Jun Jiang , Ai protocol for retrieving protein dynamic structures from two-dimensional infrared spectra, *Proceedings of the National Academy of Sciences* **122**, e2424078122 (2025).
  - [70] L. van der Maaten and G. Hinton, Visualizing high-dimensional data using t-SNE, *Journal of Machine Learning Research* **9**, 2579 (2008).
  - [71] R. A. FISHER, The use of multiple measurements in taxonomic problems, *Annals of Eugenics* **7**, 179 (1936).
  - [72] P. J. Rousseeuw, Silhouettes: A graphical aid to the interpretation and validation of cluster analysis, *Journal of Computational and Applied Mathematics* **20**, 53 (1987).
  - [73] D. L. Davies and D. W. Bouldin, A Cluster Separation Measure, *IEEE Transactions on Pattern Analysis and Machine Intelligence* **PAMI-1**, 224 (1979).
  - [74] L. McInnes, J. Healy, and S. Astels, hdbscan: Hierarchical density based clustering, *Journal of Open Source Software* **2**, 205 (2017).
  - [75] F. Pedregosa, G. Varoquaux, A. Gramfort, V. Michel, B. Thirion, O. Grisel, M. Blondel, P. Prettenhofer, R. Weiss, V. Dubourg, J. Vanderplas, A. Passos, D. Cournapeau, M. Brucher, M. Perrot, and E. Duchesnay, Scikit-learn: Machine learning in python, *Journal of Machine Learning Research* **12**, 2825 (2011).

# Supplementary Information for Exploiting correlations in multi-coincidence Coulomb explosion patterns for differentiating molecular structures using machine learning

Anbu Selvam Venkatachalam, Loren Greenman, Joshua Stallbaumer,  
Artem Rudenko, Daniel Rolles, and Huynh Van Sa Lam\*  
*James R. Macdonald Laboratory, Kansas State University, Manhattan, KS 66506, USA*  
(Dated: September 5, 2025)

In this Supplementary Information, we provide additional results and analysis details that are useful to a subset of readers, who are interested in more specialized content, but that are not essential to comprehend the main results of the article.

## CONTENTS

I. On the possibility of extending the current framework to larger molecular systems	2
A. Emerging experiment technologies	2
B. Data analysis pipelines	2
II. Additional experimental data	3
III. Additional information on the simulation model	5
A. Initial geometry	5
B. Comparison between experimental data and Coulomb explosion simulations	5
IV. Additional discussion on the machine learning analysis	7
A. Comparing different data reduction techniques	7
B. On the stochastic nature of UMAP and Random Forest Classifier	8
C. Machine-learning analysis under varied simulation conditions	9
D. Data reduction of different channels	12
1. Experimental data	12
2. Simulated data	12
E. Supporting figures for Random Forest Classification analysis	14
References	16

---

\* [huynhslam@ksu.edu](mailto:huynhslam@ksu.edu)

## I. ON THE POSSIBILITY OF EXTENDING THE CURRENT FRAMEWORK TO LARGER MOLECULAR SYSTEMS

“Complete” CEI is particularly powerful because it delivers, in every single shot, full structural information containing all the atoms in the molecule. However, capturing all ionic fragments from a total molecular breakup in coincidence—and then processing that data—is extremely challenging. The six- and eight-ion coincidences, together with the data analysis framework, demonstrated here, therefore constitute a significant advance over earlier efforts. Nevertheless, we anticipate that extending such high-fold coincidence measurements to larger molecular systems will soon become feasible, driven by experimental advances including higher repetition-rate and intense light sources, improved detector technologies, and more sophisticated analysis approaches.

### A. Emerging experiment technologies

#### Light sources

- Increased repetition rates: Given that a laser of only 3-kHz was used in our work, increasing the repetition rate of the light source will significantly enhance event statistics (e.g., 100-kHz lasers are commercially available, and the LCLS-II XFEL is currently operating at several tens of kHz and will soon be scaled up to 1-MHz operation).
- High-intensity X-ray: Using high-intensity X-ray for ionization will give a much larger population in highly charged states as compared to strong-field ionization (where low charged states are dominant as in this work). X-ray Free Electron Laser with MHz repetition rate, such as LCLS-II, can be an ideal source for this.

**Advanced detector technologies:** Using even better detectors, such as a HEX anode instead of the QUAD anode that we are using, or a pixel-independent detector (TimePix camera and similar concepts), which further improves the detection efficiency for “identical” particles (with similar  $m/q$ ). Currently, we can detect up to 4 such identical particles in a molecule. Simply using a bigger detector (e.g., 120 mm compared to the current 80-nm diameter) also helps with detection efficiently; however, the commercial availability might be limited.

**Better vacuum:** Simply having a better vacuum will allow more light intensity to be used before the data is swamped by background hits. Our vacuum is about  $1^{-10}$  mbar, which can be improved by a factor of 10 with a better pumping scheme.

Such improvements are already underway, exemplified by LCLS’s ongoing development of the DREAM Endstation [1] and next-generation detectors [2] optimized for multiparticle coincidence experiments at MHz repetition rates.

### B. Data analysis pipelines

#### Other “complete” CEI channels:

- Exploring options in data analysis, such as analyzing channels where fragments with the same  $m/q$  have different charges, will further mitigate the detection efficiency problem since those hits will arrive at the detector at different positions and different times.
- In fact, our data contains many other “complete” CEI fragmentation channels (Fig. S4). How to combine information from all these channels to obtain a better picture of the molecule and its dynamics (with a potential to also increase statistics) is of significant interest [3].

**“Incomplete” CEI channels:** Applying our method to “incomplete” events—where structural information is partially missing—is an interesting endeavor.

- For events involving incomplete breakup but complete detection, sufficient information remains to distinguish between different dynamical pathways. Our framework can handle these scenarios without modification, though it will lack specific details about the motion of atoms that do not break up.
- For events involving complete ionization but incomplete detection [such as detecting only five atomic fragments for DCE, e.g.,  $(\text{H}^+, \text{C}^+, \text{C}^+, {}^{35}\text{Cl}^+, {}^{35}\text{Cl}^+)$ ], structural information will be incomplete. Specifically, in this example, the information of one hydrogen atom is lost, causing each molecular structure to appear as two distinct clusters because the detected  $\text{H}^+$  randomly samples one of two possible hydrogen atoms. This introduces additional complexity in the analysis. Although one might attempt to reconstruct the complete molecular structure



through multivariate analysis [4], this approach would require specific assumptions about molecular geometry and the ionization process.

- In cases where structural dynamics occur predominantly within a localized region—such as intramolecular proton transfer—detecting protons along with two reference markers for the molecular frame could suffice, assuming that the carbon backbone remains largely intact.

All of these scenarios represent intriguing avenues for future research, but they lie beyond the current scope and may be explored in subsequent studies.

## II. ADDITIONAL EXPERIMENTAL DATA

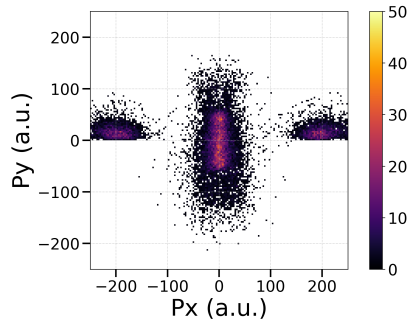


FIG. S1. Alternative Newton plot representation of the experimental Coulomb Explosion Imaging (CEI) patterns for *trans*-1,2-DCE, obtained from the six-fold coincidence channel ( $\text{H}^+$ ,  $\text{H}^+$ ,  $\text{C}^+$ ,  $\text{C}^+$ ,  $^{35}\text{Cl}^+$ ,  $^{35}\text{Cl}^+$ ). The coordinate frame for each event is defined such that the x-axis is set by the vector difference of the two  $\text{Cl}^+$  ions, while the xy-plane is established by their vector sum. Due to their back-to-back emission, the momentum sum of the two  $\text{Cl}^+$  ions is near zero, leading to an inherently less well-defined xy-reference plane.

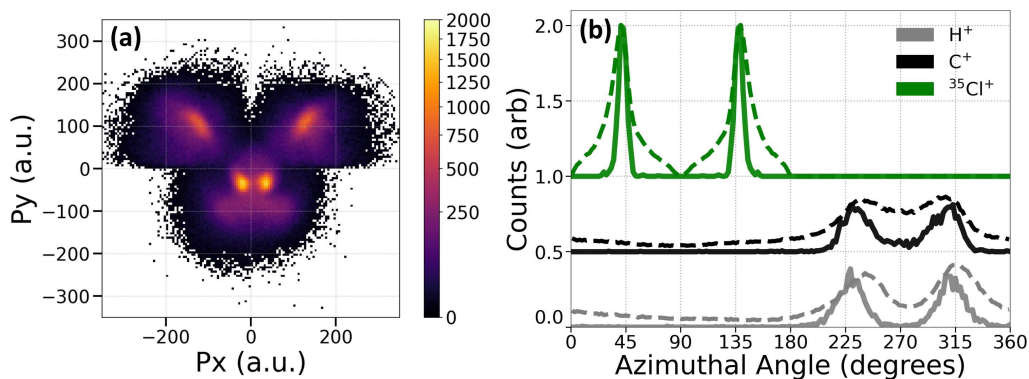


FIG. S2. (a) Newton plot for *cis*-1,2-DCE, obtained from the four-body incomplete coincidence channel ( $\text{H}^+$ ,  $\text{C}^+$ ,  $^{35}\text{Cl}^+$ ,  $^{35}\text{Cl}^+$ ). The reference frame is defined by the vector difference of the two  $\text{Cl}^+$  ions along the x-axis, with their sum lying in the upper xy-plane. (b) Yields of  $\text{H}^+$ ,  $\text{C}^+$ , and  $^{35}\text{Cl}^+$  fragments as a function of the azimuthal angle in the molecular frame. Solid lines correspond to the six-body complete coincidence fragmentation channel, while dashed lines represent the four-body incomplete coincidence channel involving  $\text{H}^+$ ,  $\text{C}^+$ , and two  $^{35}\text{Cl}^+$  ions. Distributions for  $\text{C}^+$  and  $^{35}\text{Cl}^+$  are vertically offset for clarity.

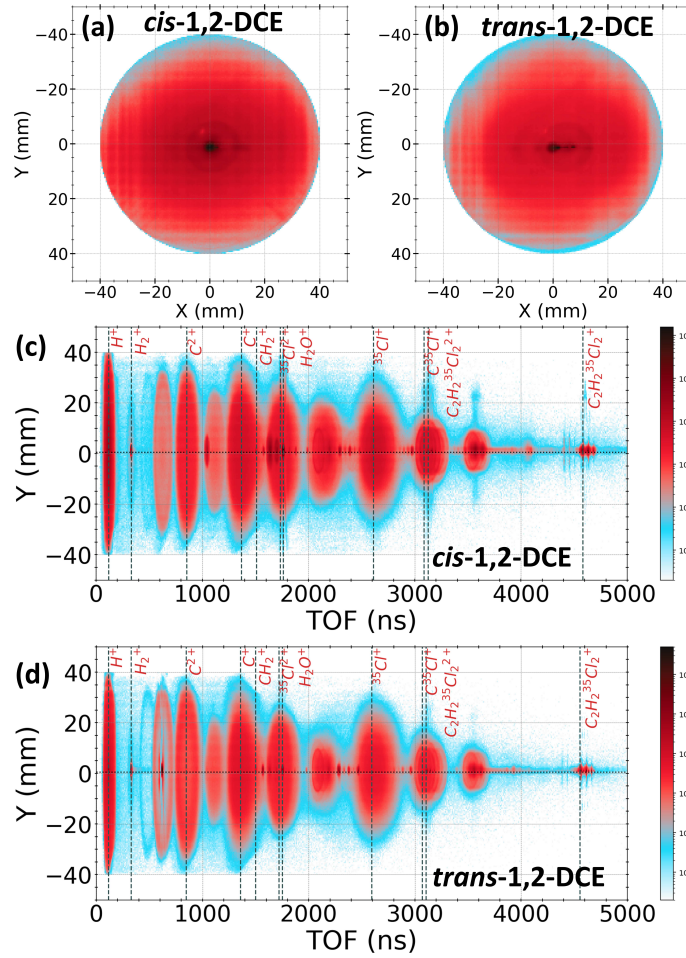


FIG. S3. Comparison of experimental ion imaging data for *cis*- and *trans*-1,2-dichloroethylene (1,2-DCE). Panels (a) and (b) show the detector-plane XY ion images integrated over all time-of-flight (TOF) values for the *cis*- and *trans*-1,2-DCE isomers, respectively. Panels (c) and (d) display the corresponding Y-TOF maps, i.e., ion yield as a function of TOF and vertical position on the detector, for *cis*- (c) and *trans*-1,2-DCE (d). Vertical dashed lines mark the major fragment ion species, and color represents intensity on a logarithmic scale.

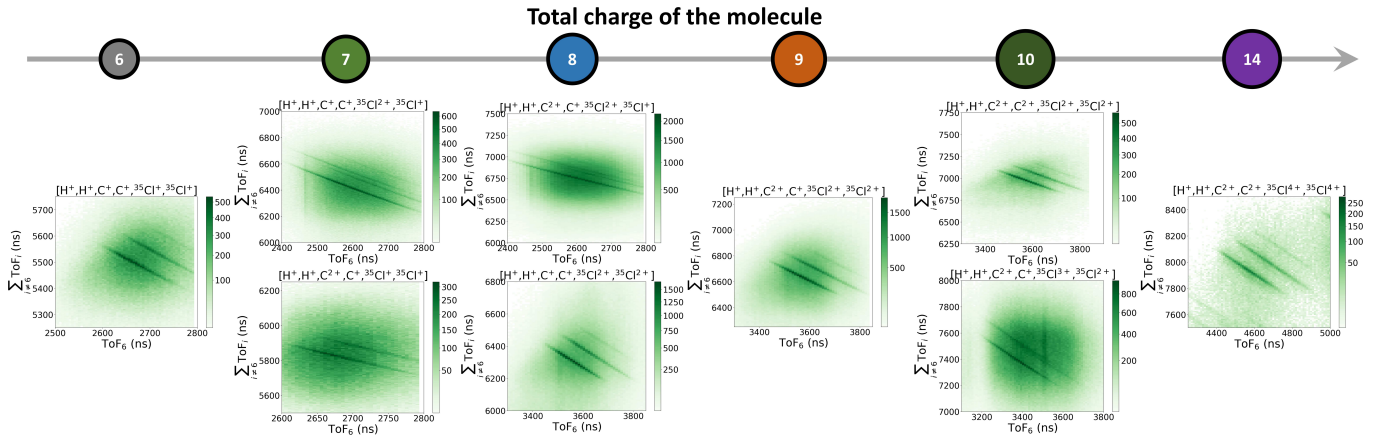


FIG. S4. Time-of-flight coincidence maps of exemplary “complete” CEI channels. The numbers on the top indicate the total charge of the final state. Multiple lines in each panel correspond to channels with different isotopes of Cl ions.

### III. ADDITIONAL INFORMATION ON THE SIMULATION MODEL

#### A. Initial geometry

TABLE I. Equilibrium geometry of *cis*-1,2-DCE optimized at the B3LYP/aug-cc-pVDZ level.

<i>cis</i> -1,2-DCE				
	Atom	x (Å)	y (Å)	z (Å)
1	C	0.66699	0.96658	0.00000
2	C	-0.66700	0.96658	0.00000
3	H	1.22333	1.90229	0.00000
4	H	-1.22333	1.90229	0.00000
5	Cl	1.66770	-0.45304	0.00000
6	Cl	-1.66770	-0.45305	0.00000

TABLE II. Equilibrium geometry of *trans*-1,2-DCE optimized at the B3LYP/aug-cc-pVDZ level.

<i>trans</i> -1,2-DCE				
	Atom	x (Å)	y (Å)	z (Å)
1	C	-0.36871	0.55424	0.00000
2	C	0.36871	-0.55424	0.00000
3	H	-1.45653	0.56855	0.00000
4	H	1.45653	-0.56855	0.00000
5	Cl	0.36871	2.13823	0.00000
6	Cl	-0.36871	-2.13823	0.00000

TABLE III. Equilibrium geometry of 1,1-DCE optimized at the B3LYP/aug-cc-pVDZ level.

1,1-DCE				
	Atom	x (Å)	y (Å)	z (Å)
1	H	0.93847	2.30932	0.00000
2	H	-0.93847	2.30932	0.00000
3	C	0.00000	1.75934	0.00000
4	C	0.00000	0.42806	0.00000
5	Cl	1.46564	-0.52185	0.00000
6	Cl	-1.46564	-0.52185	0.00000

TABLE IV. *Twisted*-1,2-DCE transient-state geometry between *cis*- and *trans*-1,2-DCE, where the C=C bond rotates 90° from the *cis*-1,2-DCE equilibrium, optimized at the B3LYP/aug-cc-pVDZ level.

<i>twisted</i> -1,2-DCE				
	Atom	x (Å)	y (Å)	z (Å)
1	C	-0.53475	1.19362	-0.31733
2	C	0.26899	0.32851	0.48543
3	H	-1.08439	1.95034	0.26295
4	H	0.15112	-0.00884	1.52174
5	Cl	-1.66406	-0.43127	-0.05612
6	Cl	1.81276	-0.22016	-0.10819

#### B. Comparison between experimental data and Coulomb explosion simulations

Fig. S5 shows a comparison between Coulomb explosion simulations using an initial Wigner distribution and the modified initial condition used in the main text in how well they can reproduce the experimental distributions of angles

between fragment momentum vectors. Fig. S6 contrasts measured versus simulated absolute momentum distributions for  $H^+$ ,  $C^+$  and  $Cl^+$  ions from the ( $H^+$ ,  $H^+$ ,  $C^+$ ,  $C^+$ ,  $Cl^+$ ,  $Cl^+$ ) channel. The simulation systematically overestimates all fragment momenta magnitudes for both isomers.

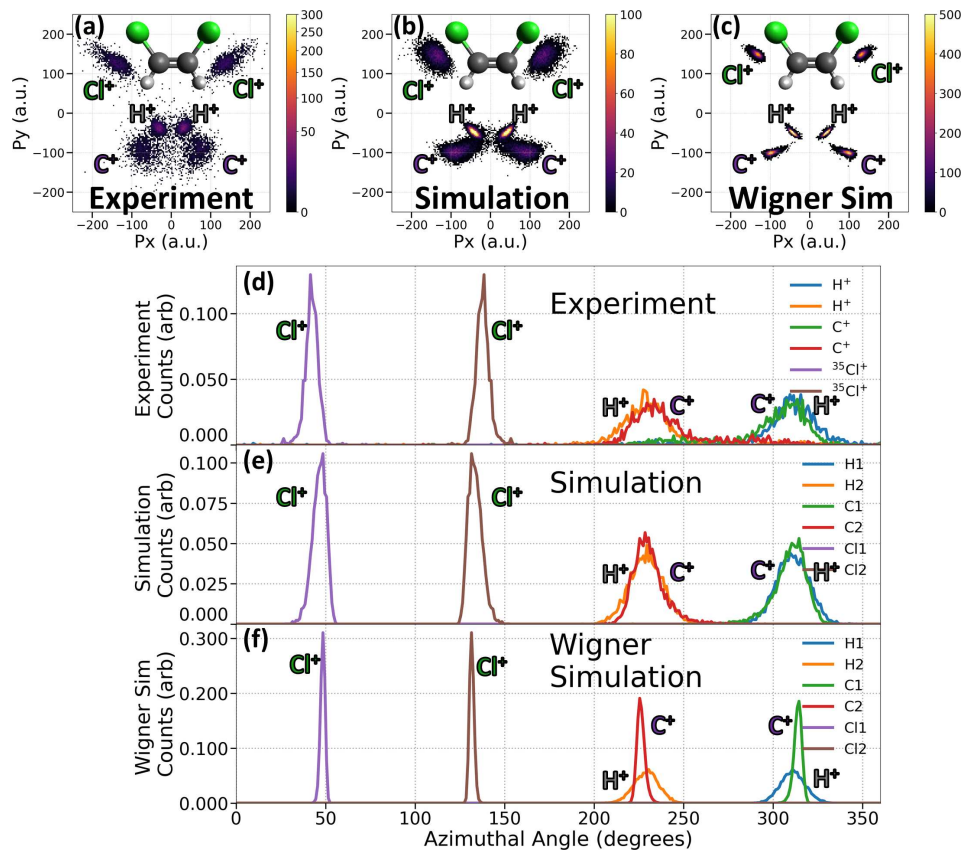


FIG. S5. CEI patterns for *cis*-1,2-DCE, showing: (a,d) experimental data, (b,e) simulation from random geometries, and (c,f) simulation from a Wigner-sampled ensemble. Panels (a), (b) and (c) show the Newton plots of momenta projected onto the  $p_x$ - $p_y$  plane. For each event, the coordinate frame is aligned such that the vector difference between the two  $Cl^+$  ions defines the  $p_x$  axis, and the vector sum of the two  $Cl^+$  lies in the upper  $p_x p_y$  plane. Panels (d), (e) and (f) show the corresponding azimuthal angle distributions, integrated over momentum magnitude, for each ion species. The azimuthal angle is measured counterclockwise from the  $p_x$  axis, and normalized to unit area.

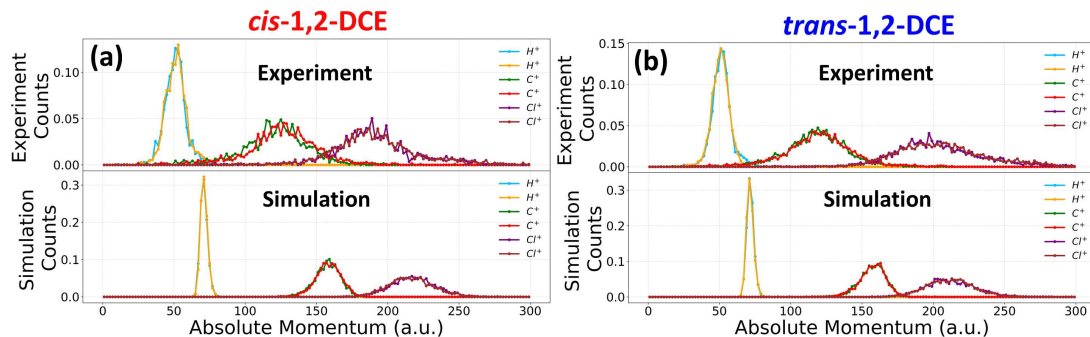


FIG. S6. Comparison between the measured (top) and simulated (bottom) absolute momenta of coincident ions from Coulomb explosion imaging of (a) *cis*-1,2-DCE and (b) *trans*-1,2-DCE molecules. The figures show the distributions for  $H^+$ ,  $C^+$ , and  $Cl^+$  ions. The simulation systematically overestimates the magnitude of the momenta of the fragments.



## IV. ADDITIONAL DISCUSSION ON THE MACHINE LEARNING ANALYSIS

### A. Comparing different data reduction techniques

In this section, we provide results from different data reduction techniques, PCA and t-SNE, for a comparison with the UMAP method shown in the main text. Technically, PCA is a linear technique that projects data onto orthogonal axes of maximal variance, preserving global structure but missing nonlinear relationships. t-SNE is a nonlinear, probabilistic method that excels at preserving local neighborhoods but can distort global distances and scales poorly to large datasets [5]. UMAP is a non-linear dimensionality reduction technique designed to preserve both local and some global structures of high-dimensional data while being computationally efficient, built upon the concepts from fuzzy topology and Riemannian geometry [6]. The results of UMAP often look quite similar to those of t-SNE because both use graph layout algorithms to arrange data in a low-dimensional space, but UMAP tends to perform better than t-SNE in the aspects mentioned above. We performed data reduction on two different data sets: one is the experimental data containing two isomers (*cis*- and *trans*-1,2 DCE) [Fig. S7], and the other is the simulated data containing four different geometries (*cis*-, *trans*-, *twisted*-1,2 DCE and 1,1-DCE) [Fig. S8].

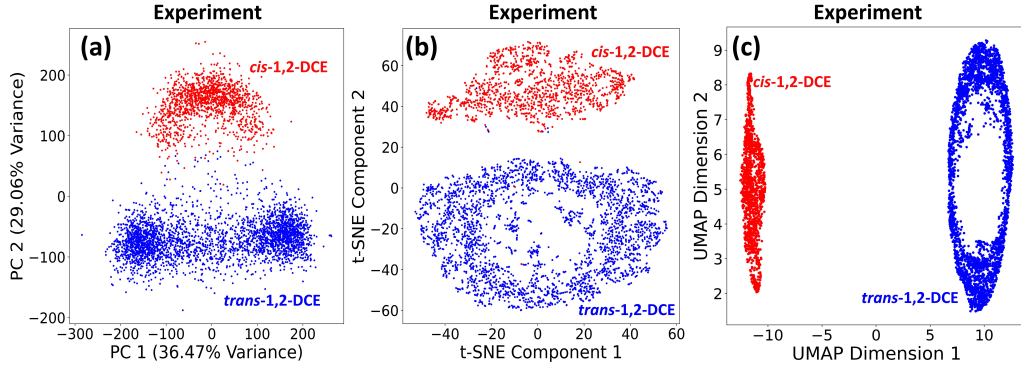


FIG. S7. Dimensionality reduction of data containing a mixture of *cis* and *trans* geometries employing (a) Principal Component Analysis (PCA), (b) t-distributed Stochastic Neighbor Embedding (t-SNE) and (c) Uniform Manifold Approximation and Projection (UMAP) with identical experimental data as inputs. The events are colored by their true labels. In this case, the data is very robust such that all these data reduction and clustering techniques can separate the two isomers in 2D representations.

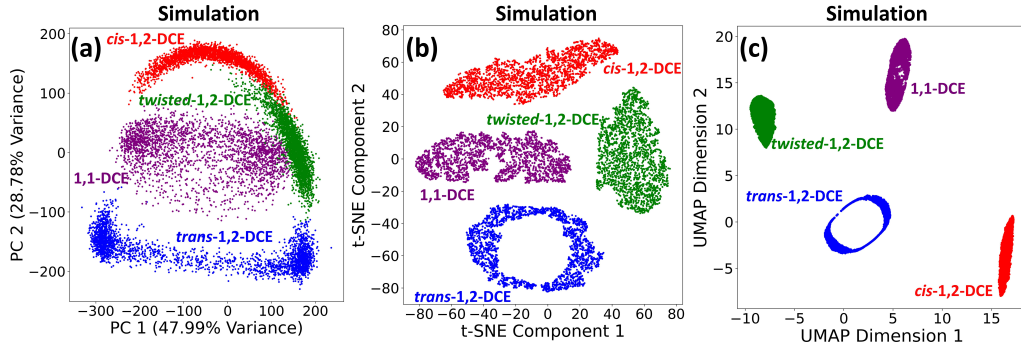


FIG. S8. Dimensionality reduction of the isomer geometries of 1,2-DCE (*cis*, *trans*, *twisted*) and 1,1-DCE using (a) Principal Component Analysis (PCA), (b) t-distributed Stochastic Neighbor Embedding (t-SNE) and (c) Uniform Manifold Approximation and Projection (UMAP) with identical simulated data as inputs. The events are colored by their true labels. This result indicates that UMAP and t-SNE are more robust than PCA in separating isomers.

UMAP visually looks better than t-SNE, and t-SNE, in turn, looks better than PCA. To qualitatively quantify the clustering quality of each dimensionality-reduction method, we computed the Silhouette Score [7] and Davies–Bouldin Index [8] for each method as shown below. The Silhouette Score measures how well each point fits within its own cluster versus other clusters, yielding a value between  $-1$  and  $1$  where higher means clearer, tighter grouping. The Davies–Bouldin Index evaluates clustering by comparing the average similarity of each cluster to its most similar

other cluster, taking values in the range  $[0, \infty)$ , with lower scores indicating more compact, well-separated clusters. The values are printed in the table below and visualized in Fig. S9.

We can see that in the case of experimental data containing two isomers, the performance of PCA and t-SNE is roughly similar, while UMAP is distinctly better. Additionally, with simulated data containing four geometries, the performance of PCA drops quickly, while t-SNE is roughly the same as before, and UMAP still yields the best result.

	Experimental data (two isomers)			Simulated data (four isomers)		
Techniques	PCA	t-SNE	UMAP	PCA	t-SNE	UMAP
Silhouette Score	0.466	0.454	0.834	0.295	0.465	0.806
Davies–Bouldin Index	0.881	0.824	0.226	1.457	0.845	0.319

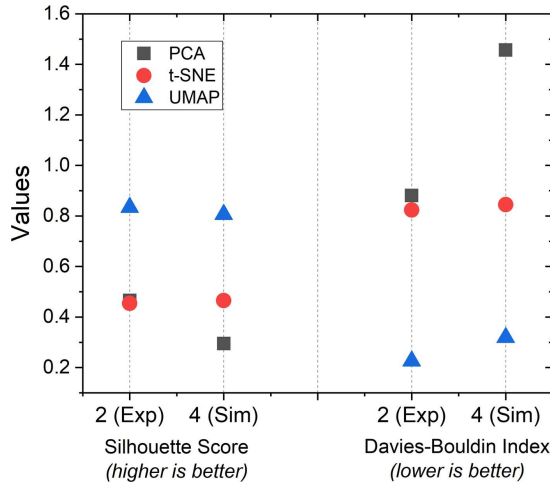


FIG. S9. Cluster metrics, Silhouette Score and Davies–Bouldin Index, calculated for different data reduction methods (PCA, t-SNE, UMAP) on experimental data containing two isomers and simulated data containing four different geometries.

In general, UMAP performs better for clustering because its nonlinear manifold approximation can uncover complex, curved structures and cluster separations (similar to t-SNE) that PCA’s straight-line projections cannot. It does this by constructing high- and low-dimensional fuzzy simplicial complexes and minimizing their cross-entropy, thereby capturing both fine-grained local connectivity and broader global trends rather than just maximizing linear variance. This is of particular importance, as shown in the next section, for supervised machine learning where simulated data can be used to guide experimental analysis. For large data sets with complicated structures such as proteins, the same conclusion was reached while comparing PCA and nonlinear techniques such as t-SNE or UMAP [9, 10]. In practice, the actual performance depends on the specific case. In cases where the data can be separated by linear projections, PCA is preferred due to its computational efficiency, simplicity, and interpretability.

### B. On the stochastic nature of UMAP and Random Forest Classifier

UMAP inherently includes a stochastic component: the “random state” hyperparameter. This parameter initializes the random number generator, which causes the UMAP result to vary between repeated runs on the same dataset. To evaluate the stability of our UMAP analysis, we repeated the dimensionality reduction procedure 100 times, each time initializing the algorithm with a different randomly assigned “random state”, and calculated the Silhouette Score [7] and Davies–Bouldin Index [8]. The resulting metrics (see table below) indicate that our UMAP analysis is highly stable and robust.

	UMAP
Silhouette Score	$0.84 \pm 0.04$
Davies–Bouldin Index	$0.22 \pm 0.05$

Similarly, due to the stochastic nature of the Random Forest Classifier—originating from its initialization with a pseudorandom number (“random state”)—its results vary slightly with different random states. To address this

variability, we repeated the classification analysis multiple times with different random states and reported the mean and standard deviation of the relative discriminative power (as shown in Fig. 4 and Fig. 5 of the main text).

### C. Machine-learning analysis under varied simulation conditions

To test the robustness of our structure identification using the dimensionality reduction approach, we examined how different spreads of possible product geometries affect the ability to differentiate between structures by considering the four scenarios listed in Table V.

TABLE V. Simulation parameters for different cases.

	Simulation parameters			
	Case I	Case II	Case III	Case IV
<i>cis</i> -1,2-DCE	0.25 Å, 0.50 eV	0.25 Å, 0.50 eV	0.25 Å, 0.50 eV	0.50 Å, 6.00 eV
<i>trans</i> -1,2-DCE	0.25 Å, 0.50 eV	0.25 Å, 0.50 eV	0.25 Å, 0.50 eV	0.50 Å, 6.00 eV
<i>twisted</i> -1,2-DCE	0.25 Å, 0.50 eV	0.50 Å, 3.00 eV	0.50 Å, 6.00 eV	0.50 Å, 6.00 eV
1,1-DCE	0.25 Å, 0.50 eV	0.50 Å, 3.00 eV	0.50 Å, 6.00 eV	0.50 Å, 6.00 eV

Case I, where the spread of all geometries is minimal, mimicking early delay times when most deposited photon energy remains as electronic excitation. Here, UMAP cleanly separates each geometry into its own cluster (Fig. 5), as extensively discussed in the main text. Case II assigns 3 eV of kinetic energy to the *twisted*-1,2-DCE and 1,1-DCE, modeling partial relaxation on the potential-energy surfaces with some energy converted into nuclear motion. In this case, the UMAP 2D projection shows partial overlap between clusters, but simulated data can be used to guide experimental analysis, as also discussed in the main text (Fig. 6).

In this section, we provide two more cases (III and IV). Case III represents complete relaxation back to the ground states (6 eV kinetic energy, corresponding to a 200 nm pump). Its classification performance (Fig. S10) matches that of Case II, with supervised UMAP + CEI cleanly separating all isomers into distinct clusters. Case IV is an extreme scenario where all geometries are widely spread to challenge the sensitivity of our analysis. As expected, overall accuracy falls (Fig. S11). However, the majority of *cis* and *trans* isomers can still be identified correctly, and the experimental data of *cis*- and *trans*-1,2-DCE (gray) show good overlap with their respective simulation clusters. Of the four isomers, *trans* displays the most distinct geometry and thus can be classified with high accuracy, whereas *cis*—whose geometry shares more similarity with 1,1-DCE [e.g.,  $\angle(\text{C}^+, \text{C}^+)$ ,  $\angle(\text{H}^+, \text{H}^+)$ ]*—*is more challenging to classify.

Finally, for a comparison, we provide results using Principal Component Analysis (PCA) and Linear Discriminant Analysis (LDA) (Fig. S12). PCA finds orthogonal axes of maximal variance while LDA optimizes axes for maximal separation between the four geometries. Both PCA and LDA only use linear combinations of the original momentum components. PCA and LDA should be compared with unsupervised UMAP and supervised UMAP, respectively. Their projections (Fig. S12) show heavy overlap between clusters, making the classification of molecular structures much more challenging. This underscores the need for high-fidelity nonlinear mapping (such as UMAP) to classify molecular structures reliably.

It is worth noting that less isomer separability [if they are still somewhat separable as in Fig. S12(b)] demands more accurate simulations to classify isomers correctly. In contrast, UMAP combined with “complete” CEI preserves both global structures (large-scale changes between different isomers) and local structural nuances (smaller-scale variation of each isomer), reducing demands on the fine-level details in the simulated data. It is also worth noting that we have not yet been able to obtain good classification using “incomplete” channels (with missing atomic ions). Although this is still a topic of investigation, it highlights the important role of “complete” CEI mode, where very rich structural information, including all atoms in the molecules, is encoded. Thus, the unique pairing of “complete” CEI and UMAP delivers reliable structure identification even under severe scatter.

### Case III

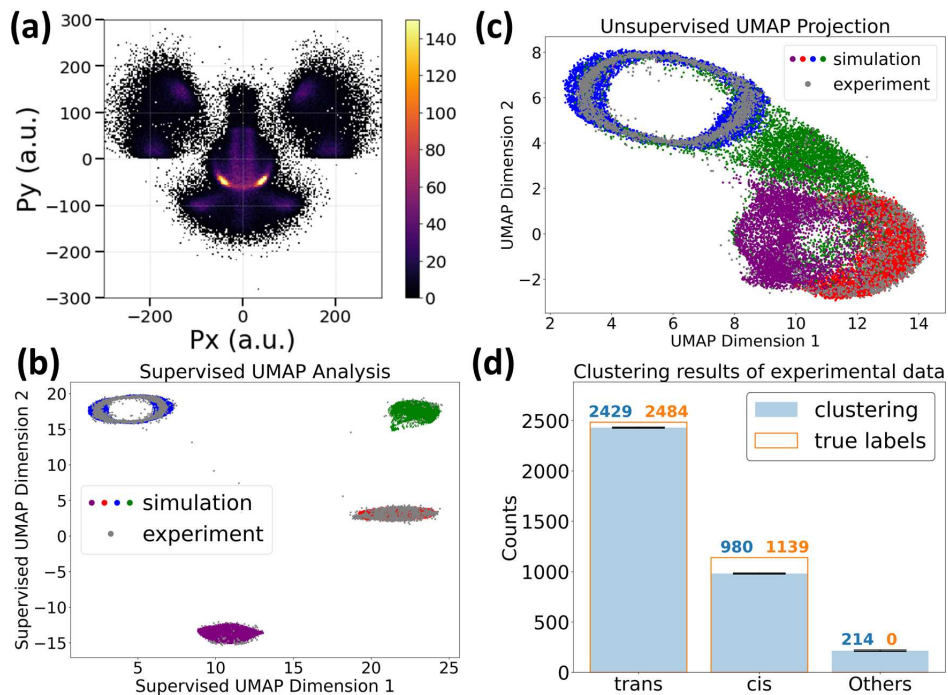


FIG. S10. Analysis of case III.

### Case IV

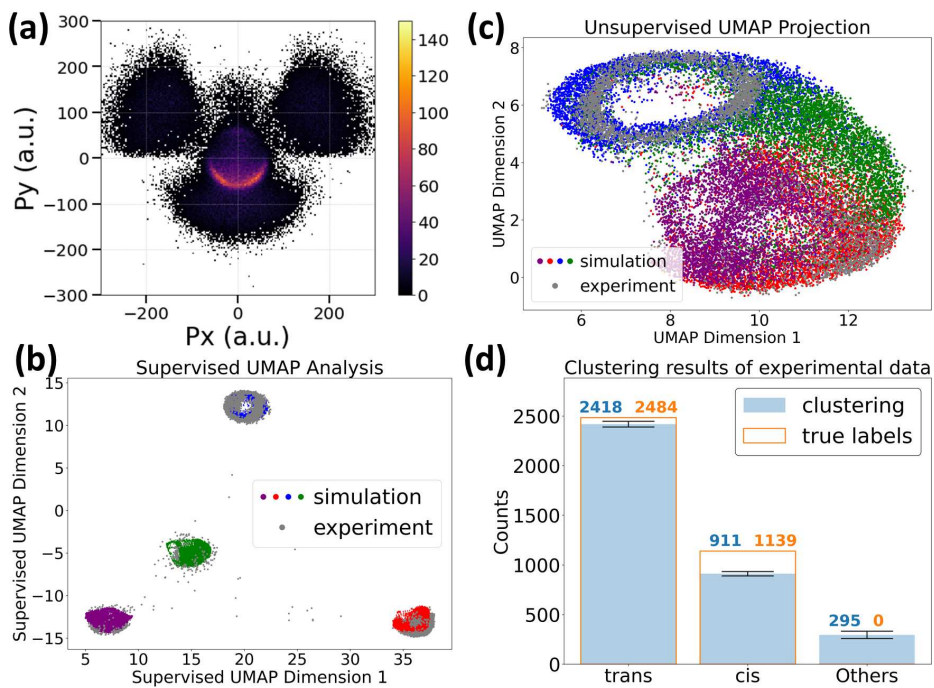


FIG. S11. Analysis of case IV.



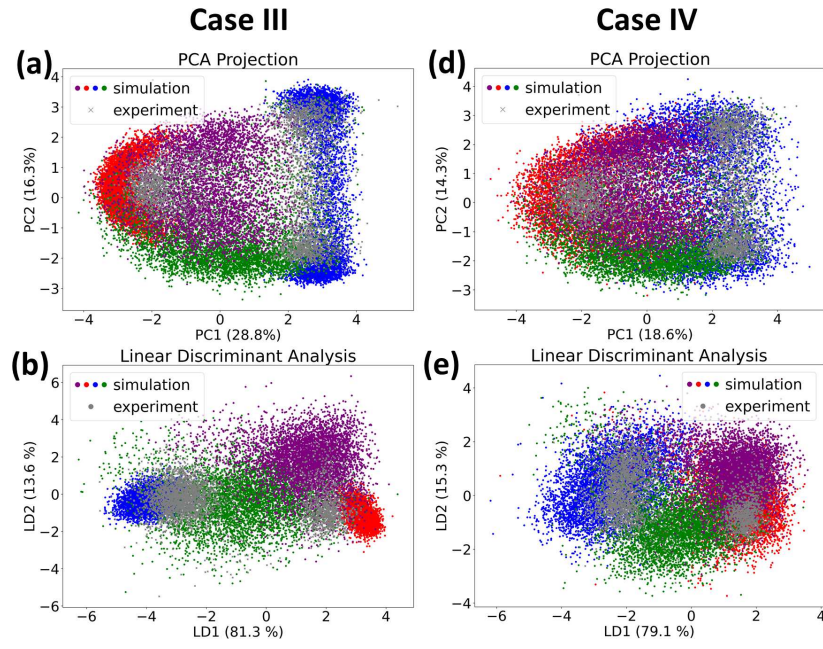


FIG. S12. Additional results using PCA and LDA.

## D. Data reduction of different channels

In this section, we examine the influence of final charge states on data reduction. The first subsection (Fig. S13) presents results from experimental data containing *cis*- and *trans*-1,2-DCE isomers. The second subsection (Fig. S14-S15) presents results from simulated data for the four geometries discussed in the main text. For simulated data, both the spatial spread and the kinetic energy imparted to the molecules were varied. Final states with higher total charges provide better separation between geometries. This improvement arises because: (1) the ratio between the width of the momentum distribution to the momentum magnitude becomes smaller, producing more distinct features, and (2) Coincidence events with more fragments contain richer structural information.

### 1. Experimental data

In Fig. S13, we evaluate the data reduction across three representative fragmentation channels. The Newton plots (a–c), UMAP embeddings (d–f), and distributions of angle between the two chlorine fragments (g–i) all show that fragmentation channels with higher total final-state charges yield clearer separation between geometries.

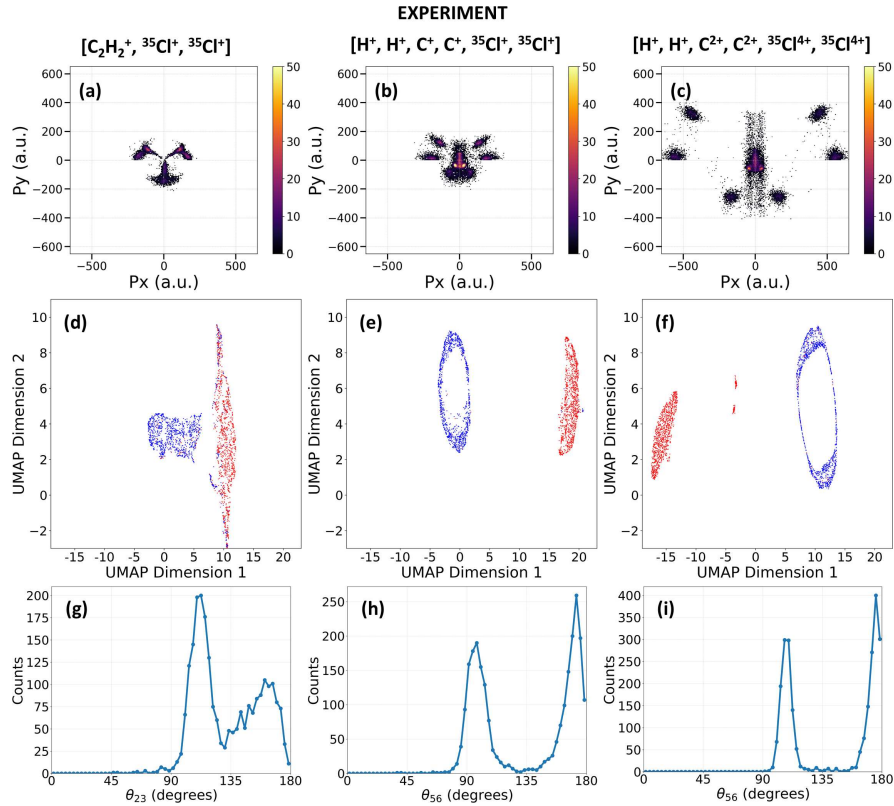


FIG. S13. Experimental data reduction for three fragmentation channels. (a–c) Newton plots in the molecular plane the three channels: (a) three-body, total charge 3+ ( $\text{C}_2\text{H}_2^+, {}^{35}\text{Cl}^+, {}^{35}\text{Cl}^+$ ); (b) six-body, total charge 6+ ( $\text{H}^+, \text{H}^+, \text{C}^+, \text{C}^+, {}^{35}\text{Cl}^+, {}^{35}\text{Cl}^+$ ); (c) six-body, total charge 14+ ( $\text{H}^+, \text{H}^+, \text{C}^{2+}, \text{C}^{2+}, {}^{35}\text{Cl}^{4+}, {}^{35}\text{Cl}^{4+}$ ). (d–f) Two-dimensional Uniform Manifold Approximation and Projection (UMAP) embeddings corresponding to (a–c). (g–i) Distributions of the angle between the two chlorine ions for (a–c). The number of events is fixed across channels, and axis limits are matched for all Newton plots and UMAP panels to enable direct comparison. In UMAP embeddings, points are colored by their true geometry labels.

### 2. Simulated data

In this section, we systematically broadened the initial real-space distributions and increased the kinetic energy for *twisted*-1,2-DCE and 1,1-DCE in the simulation. Across conditions, higher total final-state charge yields more robust

separations of geometries in the UMAP embeddings: clusters in the +14 channel remain distinct as noise or energy grows, whereas the +6 channel progressively overlaps. In all plots, points are colored by their true geometry labels.

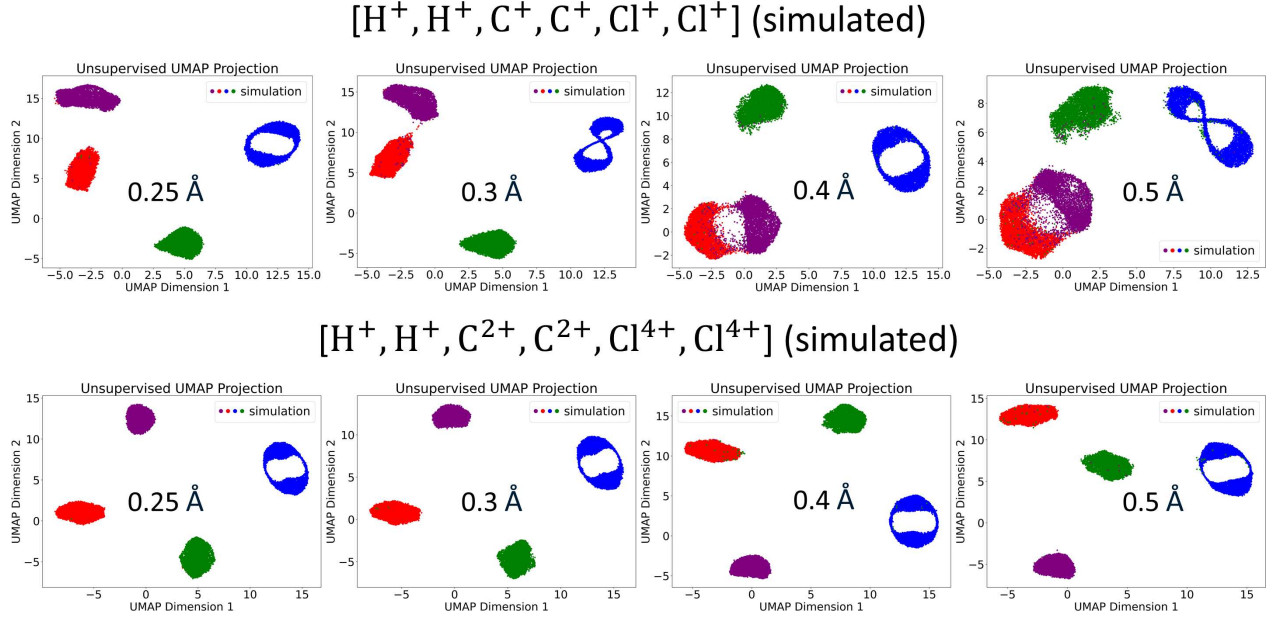


FIG. S14. Comparison between two fragmentation channels with a total final charge of +6 (top) and +14 (bottom). Simulation parameters for *cis* and *trans* were fixed at 0.5 Å and 0.5 eV. For *twisted*-1,2-DCE and 1,1-DCE, the kinetic energy was set to 0.5 eV, with spatial deviations increasing from 0.25 Å to 0.5 Å (left to right). The +6 channel starts to show overlap between *cis*-1,2-DCE and 1,1-DCE in the last two columns, while the +14 channel maintains clear separation throughout. The events are colored by their true labels.

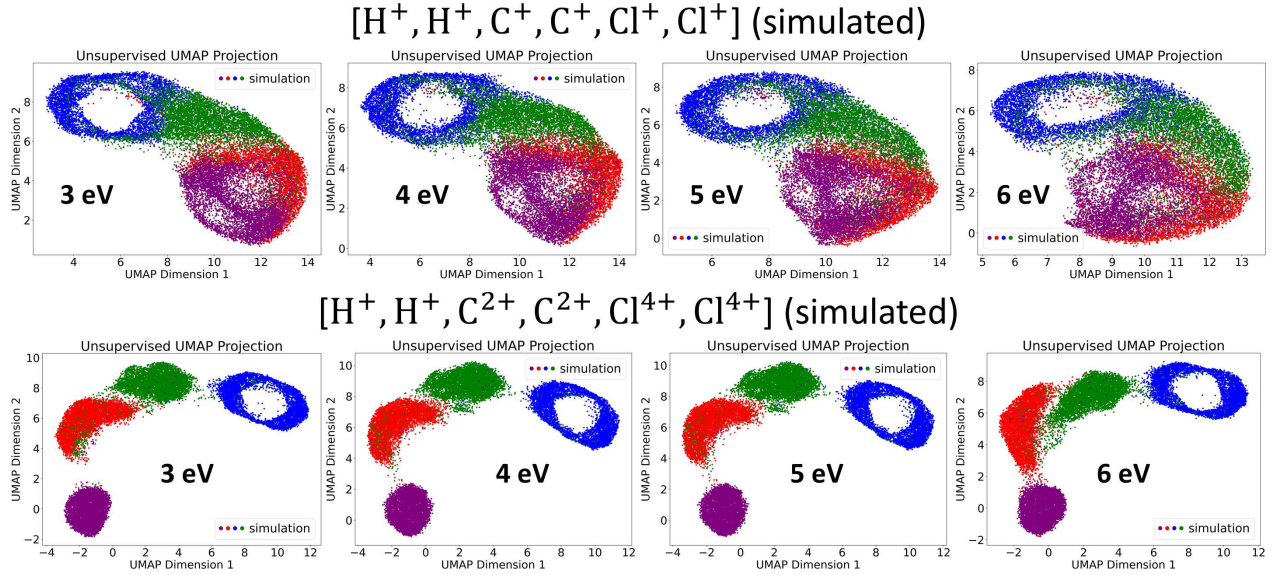


FIG. S15. Comparison between the same +6 (top) and +14 (bottom) channels with varying the kinetic energy from 3 eV to 6 eV (left to right). For all geometries, the spatial deviation was kept at 0.5 Å while the kinetic energy was varied from 3 eV to 6 eV (left to right). The +6 channel exhibits substantial overlap between geometries, whereas the +14 channel shows consistently well-separated clusters. In all simulations, points are colored by their true geometry labels.

### E. Supporting figures for Random Forest Classification analysis

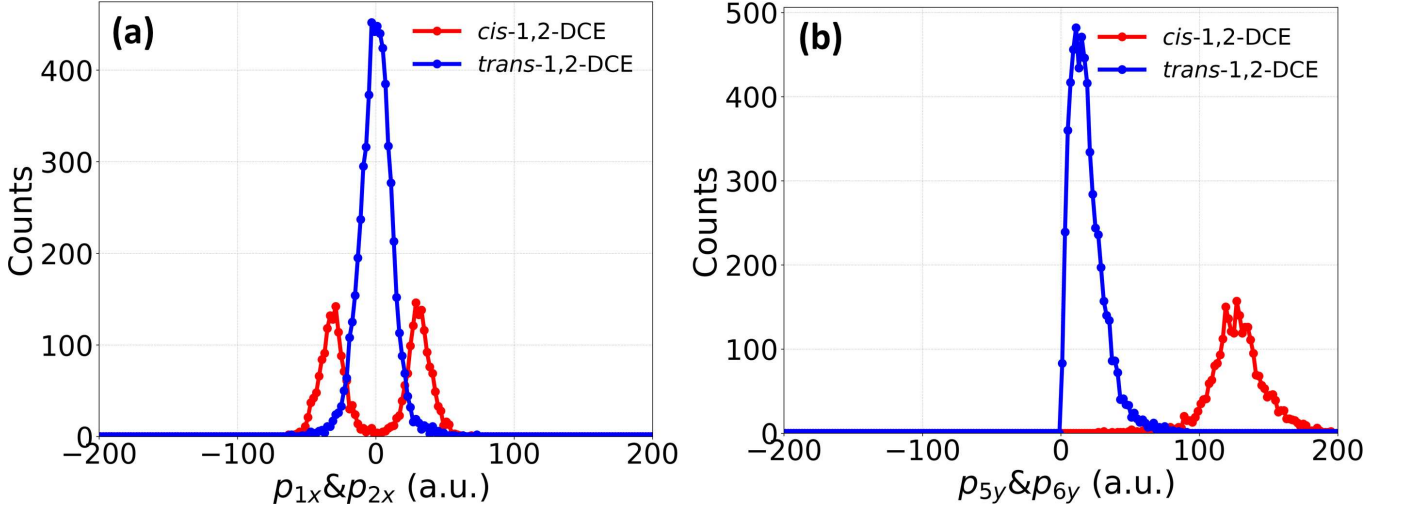


FIG. S16. Momentum distributions of the chlorine and proton fragments in the *cis* and *trans*-1,2-DCE isomers. (a) Horizontal momentum component of protons ( $p_{1x}$  and  $p_{2x}$ ). (b) Vertical momentum component of chlorine ions ( $p_{5y}$  and  $p_{6y}$ ). The separation of the distributions for *cis* and *trans* reflects the structural differences between the isomers and demonstrates that these momentum components are good discriminators for the two isomers, as quantified by our analysis using the Random Forest classifier model.

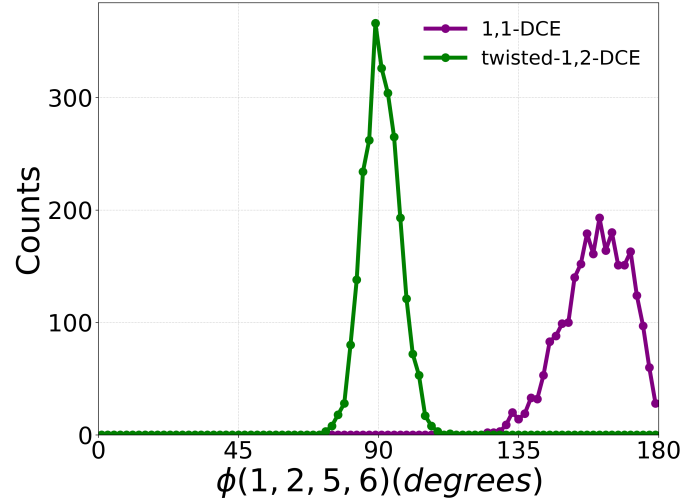


FIG. S17. 1D distributions of  $\phi_{1256}$  — the angle between two planes formed by the ( $H^+$ ,  $H^+$ ) and ( $Cl^+$ ,  $Cl^+$ ) momentum vectors. This angle serves as a key distinguishing feature between *twisted*-1,2-DCE and 1,1-DCE, showing two well-separated distributions.



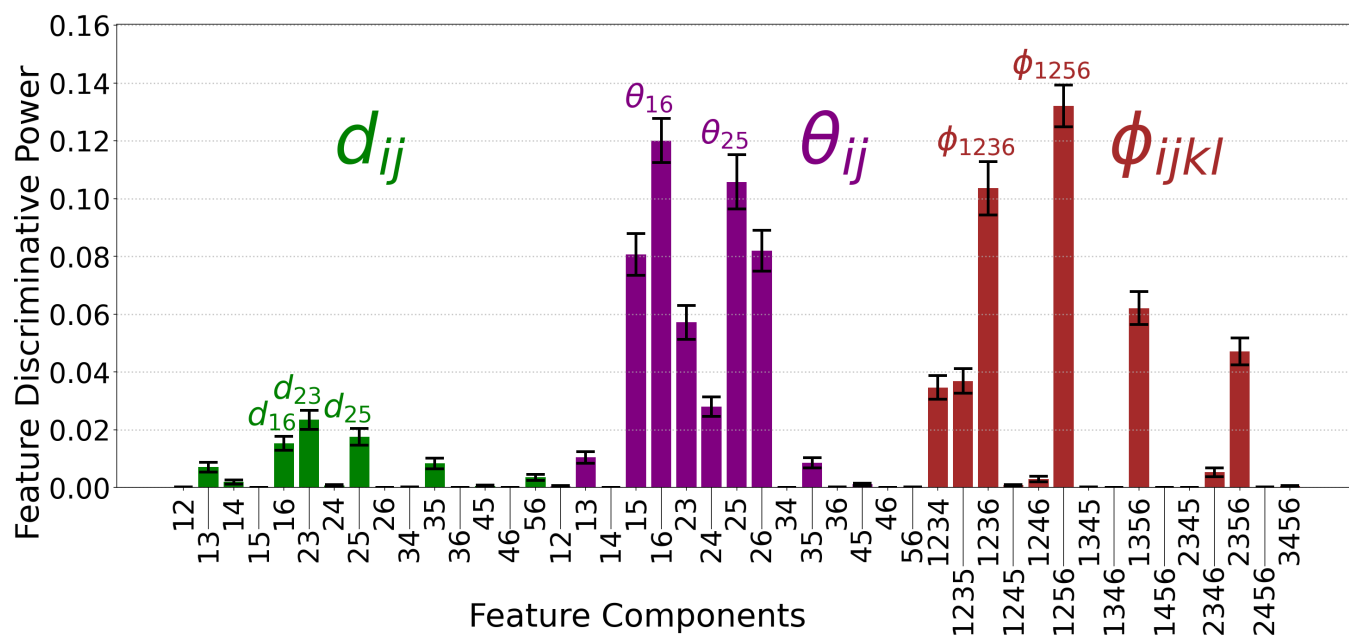


FIG. S18. Discriminative power analysis using a Random Forest classifier model applied to distinguish between the *twisted-1,2*-DCE and *1,1*-DCE isomers. The bar heights indicate the relative discriminative power of different features. The strongest discriminator in this case is  $\phi_{1256}$  — the angle between two planes formed by protons and chlorine ions.

- 
- [1] P. Walter, M. Holmes, R. Obaid, L. Amores, X. Cheng, J. P. Cryan, J. M. Glowina, X. Li, M.-F. Lin, M. L. Ng, J. Robinson, N. Shivaram, J. Yin, D. Fritz, J. James, J.-C. Castagna, and T. Osipov, The DREAM Endstation at the Linac Coherent Light Source, *Applied Sciences* **12**, 10534 (2022).
  - [2] B. Markovic, C. Bakalis, G. Blaj, X. Defay, D. Doering, A. Gupta, J. Hasi, C. Kenney, P. King, A. Pena-Perez, B. Reese, L. Rota, L. Ruckman, J. Segal, T. Driver, J. Cryan, C. Hansson, and A. Dragone, SparkPix-T: Spatial and Time Resolving Front-End ASIC with MHz-Rate Information Extraction for Momentum Spectroscopy at LCLS-II, in *2023 IEEE Nuclear Science Symposium, Medical Imaging Conference and International Symposium on Room-Temperature Semiconductor Detectors (NSS MIC RTSD)* (2023) pp. 1–1, iSSN: 2577-0829.
  - [3] X. Li, R. Boll, P. Vindel-Zandbergen, J. González-Vázquez, D. E. Rivas, S. Bhattacharyya, K. Borne, K. Chen, A. De Fanis, B. Erk, R. Forbes, A. E. Green, M. Ilchen, B. Kaderiya, E. Kuk, H. V. S. Lam, T. Mazza, T. Mullins, B. Senfftleben, F. Trinter, S. Usenko, A. S. Venkatachalam, E. Wang, J. P. Cryan, M. Meyer, T. Jahnke, P. J. Ho, D. Rolles, and A. Rudenko, Imaging a light-induced molecular elimination reaction with an X-ray free-electron laser, *Nat Commun* **16**, 7006 (2025).
  - [4] B. Richard, R. Boll, S. Banerjee, J. M. Schäfer, Z. Jurek, G. Kastirke, K. Fehre, M. S. Schöffler, N. Anders, T. M. Baumann, S. Eckart, B. Erk, A. De Fanis, R. Dörner, S. Grundmann, P. Grychtol, M. Hofmann, M. Ilchen, M. Kircher, K. Kubicek, M. Kunitski, X. Li, T. Mazza, S. Meister, N. Melzer, J. Montano, V. Music, Y. Ovcharenko, C. Passow, A. Pier, N. Rennhack, J. Rist, D. E. Rivas, D. Rolles, I. Schlichting, L. P. H. Schmidt, P. Schmidt, D. Trabert, F. Trinter, R. Wagner, P. Walter, P. Ziolkowski, A. Rudenko, M. Meyer, R. Santra, L. Inhester, and T. Jahnke, Imaging collective quantum fluctuations of the structure of a complex molecule, *Science* **389**, 650 (2025).
  - [5] L. van der Maaten and G. Hinton, Visualizing high-dimensional data using t-SNE, *Journal of Machine Learning Research* **9**, 2579 (2008).
  - [6] L. McInnes, J. Healy, and J. Melville, UMAP: Uniform Manifold Approximation and Projection for Dimension Reduction (2018), [arXiv:1802.03426 \[stat.ML\]](https://arxiv.org/abs/1802.03426).
  - [7] P. J. Rousseeuw, Silhouettes: A graphical aid to the interpretation and validation of cluster analysis, *Journal of Computational and Applied Mathematics* **20**, 53 (1987).
  - [8] D. L. Davies and D. W. Bouldin, A Cluster Separation Measure, *IEEE Transactions on Pattern Analysis and Machine Intelligence* **PAMI-1**, 224 (1979).
  - [9] T. André, I. Dawod, S. Cardoch, E. De Santis, N. Timneanu, and C. Caleman, Protein structure classification based on x-ray-laser-induced coulomb explosion, *Phys. Rev. Lett.* **134**, 128403 (2025).
  - [10] M. W. Dorrity, L. M. Saunders, C. Queitsch, S. Fields, and C. Trapnell, Dimensionality reduction by UMAP to visualize physical and genetic interactions, *Nat Commun* **11**, 1537 (2020).